Editorial summary:

Hydroxyl radicals are reactive species capable of water purification and disinfection, although their generation, particularly through renewable approaches, is challenging. Now, low-valent Au on potassium-incorporated carbon nitride has been shown to produce hydroxyl radicals upon solar illumination and to provide high water disinfection rates.

Peer review Information:

Nature Chemistry thanks Xinchen Wang and the other, anonymous, reviewers for their contribution to the peer review of this work.

Inventory of Supporting Information

Manuscript #: NCHEM-23071367B

Corresponding author name(s): Bin Liu

1. Extended Data

Figure or Table # Please group Extended Data items by type, in sequential order. Total number of items (Figs. + Tables) must not exceed 10.	Figure/Table title One sentence only	Filename Whole original file name including extension. i.e.: Smith_ED_Fig1.jpg	Figure/Table Legend If you are citing a reference for the first time in these legends, please include all new references in the main text Methods References section, and carry on the numbering from the main References section of the paper. If your paper does not have a Methods section, include all new references at the end of the main Reference list.
Extended Data Fig. 1	**High-resolution XPS spectra to determine the surface chemical states of Au.**	Extended Data Fig. 1.eps	**High-resolution XPS spectra to determine the surface chemical states of Au. a**, Au (4 $f_{7/2}$ and 4 $f_{5/2}$) spectra in AuPCN and AuKPCN. **b**, Au (4 $f_{7/2}$) spectrum in Au foil as a reference.
Extended Data Fig. 2	**Solid state NMR analysis of PCN.**	Extended Data Fig. 2. eps	**Solid state NMR analysis of PCN. a**, Groups of C and N atoms marked with symbols in PCN. **b**, ^{13}C solid-state NMR spectrum of PCN. Inset shows the enlarged spectrum. **c**, Calculated ^{13}C NMR chemical shifts for a melon model (neutral). **d**, ^{15}N solid-state NMR spectrum of PCN. Inset shows the enlarged spectrum. **e**, Calculated ^{15}N NMR chemical shifts for a melon model (neutral).

Extended Data Fig. 3	**Solid state NMR analysis of KPCN.**	Extended Data Fig. 3. eps	**Solid state NMR analysis of KPCN. a**, Groups of C and N atoms marked with symbols in KPCN. **b**, ^{13}C solid-state NMR spectrum of KPCN. Inset shows the enlarged spectrum. **c**, Calculated ^{13}C NMR chemical shifts for a K-PHI model (neutral). **d**, ^{15}N solid-state NMR spectrum of KPCN. Inset shows the enlarged spectrum. **e**, Calculated ^{15}N NMR chemical shifts for a K-PHI model (neutral).
Extended Data Fig. 4	**Solid state NMR analysis of AuKPCN.**	Extended Data Fig. 4. eps	**Solid state NMR analysis of AuKPCN. a**, Groups of C and N atoms marked with symbols in AuKPCN. **b**, ^{13}C solid-state NMR spectrum of AuKPCN. Inset shows the enlarged spectrum. **c**, Calculated ^{13}C NMR chemical shifts for Au on K-PHI framework (neutral). **d**, ^{15}N solid-state NMR spectrum of AuKPCN. Inset shows the enlarged spectrum. **e**, Calculated ^{15}N NMR chemical shifts for Au on a K-PHI model (neutral). The simulation of Au was conducted at SDD level.
Extended Data Fig. 5	***In-situ* XPS spectra for AuPCN and AuKPCN recorded in dark and under visible light illumination.**	Extended Data Fig. 5. eps	***In-situ* XPS spectra for AuPCN and AuKPCN recorded in dark and under visible light illumination. a**, High-resolution XPS spectra of AuPCN: Au $4f_{7/2}$ and Au $4f_{5/2}$ under light irradiation for 5 min (up) and 10 min (down). **b**, High-resolution XPS spectra of AuKPCN: Au $4f_{7/2}$ and Au $4f_{5/2}$ under light irradiation for 5 min (up) and 10 min (down). **c**, Chemical state change in AuKPCN and AuPCN during the *In-situ* XPS experiment.
Extended Data Fig. 6	**Surface hydrophilicity evolution.**	Extended Data Fig. 6. eps	**Surface hydrophilicity evolution. a-d**, Contact angle images of PCN (**a**), KPCN (**b**), AuPCN (**c**) and AuKPCN (**d**) under light irradiation. **e-f**, The changing tendency of contact angles. **e-f**, Changes in contact angle measurements with illumination for (**e**) polymeric carbon nitride samples and (**f**) commercialized TiO2 (Dr. Ohno). Inset, Contact angle measurements for

			commercialized TiO2 (Dr. Ohno) under short light irradiation times.

Do not insert additional rows - total number of Extended Data items must not exceed 10.

1. Supplementary Information:

A. PDF Files

Item	Present?	Filename Whole original file name including extension. i.e.: Smith_SI.pdf. The extension must be .pdf	A brief, numerical description of file contents. i.e.: *Supplementary Figures 1-4, Supplementary Discussion, and Supplementary Tables 1-4.*
Supplementary Information	Yes		Supplementary Scheme 1; Supplementary Figures 1-56; Supplementary Tables1-17; Supplementary Notes 1-11
Reporting Summary	No		
Peer Review Information	No	*OFFICE USE ONLY*	

B. Additional Supplementary Files

Type	Number Each type of file (Table, Video, etc.) should be numbered from 1 onwards. Multiple files of the same type should be listed in sequence, i.e.: Supplementary Video 1, Supplementary Video 2, etc.	Filename Whole original file name including extension. i.e.: *Smith_ Supplementary_Video_1.mov*	Legend or Descriptive Caption Describe the contents of the file

Supplementary Video	1	Supplementary_Videos_1_ReferencePCN.mp4	Hydrophobic PCN.
Supplementary Video	2	Supplementary_Videos_2_ReferenceAuPCN	Hydrophobic AuPCN.
Supplementary Video	3	Supplementary_Videos_3_ReferenceKPCN	Hydrophobic KPCN.
Supplementary Video	4	Supplementary_Videos_4_Superhydrophilic_AuKPCN	Super hydrophilic AuKPCN
Supplementary Video	5	Supplementary_Videos_5_Animations for Supplementary Figure 39	Animations for vibration of simulated FTIR.
Supplementary Data	1	Supplementary_Data.zip	Source Data of Supplementary Figures.

Add rows as needed to accommodate the number of files.

3. Source Data

Parent Figure or Table	Filename Whole original file name including extension. i.e.: *Smith_SourceData_Fig1.xls,* or *Smith_ Unmodified_Gels_Fig1.pdf*	Data description i.e.: Unprocessed western Blots and/or gels, Statistical Source Data, etc.
Source Data Fig. 1	Figure1.xlsx	Source Data of Figure 1.
Source Data Fig. 2	Figure2.rar	Source Data of Figure 2.
Source Data Fig. 3	Figure3.rar	Source Data of Figure 3.

Source Data Fig. 4	Figure4.xlsx	Source Data of Figure 4.
Source Data Fig. 5	Figure5.xlsx	Source Data of Figure 5.
Source Data Extended Data Fig. 1	Extended Data1.xlsx	Source Data of Extended Data Figure 1.
Source Data Extended Data Fig. 2	Extended Data2.xlsx	Source Data of Extended Data Figure 2.
Source Data Extended Data Fig. 3	Extended Data3.xlsx	Source Data of Extended Data Figure 3.
Source Data Extended Data Fig. 4	Extended Data4.xlsx	Source Data of Extended Data Figure 4.
Source Data Extended Data Fig. 5	Extended Data5.xlsx	Source Data of Extended Data Figure 5.
Source Data Extended Data Fig. 6	Extended Data6.xlsx	Source Data of Extended Data Figure 6.

Atomically dispersed low-valent Au boosts photocatalytic hydroxyl radical production

Zhenyuan Teng,[1,10] Hongbin Yang,[1,10] Qitao Zhang,[2,10] Wenan Cai,[3] Ying-Rui Lu,[4] Kosaku Kato,[5] Zhenzong Zhang,[6] Jie Ding,[1] Han Sun,[7] Sixiao Liu,[8] Chengyin Wang,[8] Peng Chen,[6] Akira Yamakata,[5] Ting-Shan Chan,[4] Chenliang Su,[2,*] Teruhisa Ohno,[3,*] and Bin Liu[1,9,*]

[1]Department of Materials Science and Engineering, City University of Hong Kong, Tat Chee Avenue, Kowloon, Hong Kong SAR 999007, China

[2]Institute of Microscale Optoelectronics, Shenzhen University, Shenzhen 518060, China

[3]Department of Applied Chemistry, Faculty of Engineering, Kyushu Institute of Technology, Kitakyushu 804-8550, Japan

[4]National Synchrotron Radiation Research Center, Hsinchu 30076, Taiwan

[5]Department of Chemistry, Okayama University, 3-1-1 Tsushima-naka, Kita-ku, Okayama 700-8530, Japan

[6]School of Chemistry, Chemical Engineering and Biotechnology, Nanyang Technological University, Singapore 637459, Singapore

[7]The Third Affiliated Hospital of Soochow University, 185 Juqian Street, Changzhou 213003, China

[8]College of Chemistry and Chemical Engineering, Yangzhou University, 180 Si-Wang-Ting Road, Yangzhou 225002, China

[9]Department of Chemistry, Hong Kong Institute of Clean Energy (HKICE) & Center of Super-Diamond and Advanced Films (COSDAF), City University of Hong Kong, Hong Kong SAR 999077, China

[10]These authors contributed equally.

Email: chmsuc@szu.edu.cn (C. Su), tohno@che.kyutech.ac.jp (T. Ohno) and bliu48@cityu.edu.hk (B. Liu)

Abstract

Providing affordable, safe drinking water and universal sanitation poses a grand societal challenge. In this work, we developed atomically dispersed Au on potassium-incorporated polymeric carbon nitride material that could simultaneously boost photocatalytic generation of ·OH and H_2O_2 with an apparent quantum efficiency over 85% at 420 nm. Potassium introduction into the poly(heptazine imide) matrix formed strong K–N bonds and rendered Au with an oxidation

number close to 0. Extensive experimental characterization and computational simulations revealed that the low-valent Au altered the materials' band structure to trap highly localized holes produced under photoexcitation. These highly localized holes could boost the $1e^-$ water oxidation reaction to form highly oxidative ·OH and simultaneously dissociate the hydrogen atom in H_2O, which greatly promoted the reduction of oxygen to H_2O_2. The photogenerated ·OH led to an efficiency enhancement for visible-light-response superhydrophilicity. Furthermore, photo-illumination in an onsite fixed-bed reactor could disinfect water at a rate of 66 L H_2O m^{-2} day^{-1}.

Introduction

Hydroxyl radicals (·OH) are regarded as one of the most important reactive oxygen species (ROS) for photosynthesis and energy/environment chemistry[1]. The generation of ·OH is a key topic of interest in energy research[1]. For environment chemistry, ·OH radicals also work as the most oxidative ROS for water purification and disinfection[2]. The global water crisis has been drastically aggravated by the COVID-19 pandemic[3, 4], a 40 percent shortfall is estimated in freshwater resource by 2030 coupled with a rising world population[3, 4]. A photocatalytic system with the highest generation rate of ·OH is most desirable for highly efficient onsite solar water disinfection for affordable drinking water[5, 6]. Combining artificial photosynthesis of H_2O_2 via $2e^-$ oxygen reduction reaction (ORR)[7-11] and Fenton reaction offers an indirect approach for ·OH production at the reduction side of a photocatalyst because of the almost unity efficiency of Fenton reaction for the conversion of ·OH from H_2O_2 ($2h\nu$ can generate one ·OH, eq. 3)[12, 13]. On the other hand, at the oxidation side, the $1e^-$ water oxidation reaction (WOR) offers the most efficient route for direct ·OH generation because one h^+ can generate one ·OH (Figure 1a, Supplementary Scheme 1, Supplementary Table 1)[14-16].

Unfortunately, the external quantum efficiencies of producing ·OH via photocatalytic WOR over traditional inorganic semiconductors (e.g., TiO_2) are less than 6%[5]. The redox potentials of photogenerated holes in the valence band of traditional inorganic semiconductors are sufficient to drive photocatalytic $4e^-$, $2e^-$, and $1e^-$ WOR (eq. 1-3), with oxides and nitrides having values of approximately 3.0 V and 2.0 V (vs. NHE), respectively[17]. While $1e^-$ WOR has faster kinetics than $4e^-$ and $2e^-$ WOR, the latter two are thermodynamically more favorable due to the larger potential difference between the reaction and photogenerated holes. Achieving highly selective photocatalytic $1e^-$ WOR requires an oxidative site with a highly restricted charge transfer number (n). In contrast to traditional inorganic semiconductors, where charge transfer occurs continuously,

organic semiconductors can realize discontinuous charge transfer via trapping and de-trapping[18-20]. Immobilizing isolated metallic sites on organic semiconductors has been shown possible to tune the charge transfer properties[10, 18], which may result in ideal charge transfer numbers for targeted reactions.

$$2H_2O\ (l) \rightarrow O_2\ (g) + 4H^+\ (aq) + 4e^-\ (0.82\ V\ vs.\ RHE,\ pH = 7) \quad (1)$$

$$2H_2O\ (l) \rightarrow H_2O_2\ (l) + 2H^+ + 2e^-\ (aq)\ (1.35\ V\ vs.\ RHE,\ pH = 7) \quad (2)$$

$$H_2O\ (l) \rightarrow HO\cdot\ (aq) + H^+ + e^-\ (aq)\ (1.97\ V\ vs.\ RHE,\ pH = 7) \quad (3)$$

Poly(heptazine imide) is a highly crystalline polymeric carbon nitride (PCN) that exhibits thermodynamically favorable redox potential (1.8~2.0 V vs. RHE) for $1e^-$ WOR (eq. 3)[18, 20]. Thus, building isolated metallic sites over poly(heptazine imide) with only one valence electron that can be easily excited to leave a highly localized hole is particularly desired to restrict the charge transfer number (n = 1) for highly selective photocatalytic $1e^-$ WOR. The group 11 elements (e.g., Cu, Ag and Au) have the s orbital filled by one electron and d^{10} orbitals fully filled by electrons[21]. If the electron in the s orbital at the single-metallic site is excited to the conduction band, the positive charge can lead to the formation of a localized hole. But the oxidation number of the atomically dispersed sites on a PCN framework must be regulated to extremely low so that the electron of the s orbital can remain confined at the isolated metallic side at the ground state, and then form a highly concentrated hole during photoexcitation (Figure 1b). The polarization of a chemical bond is usually determined by the electronegativity of atoms. In the single atom catalyst fixed on carbon nitride, the interactions between C, N and the introduced group 11 element have to be carefully manipulated to achieve a low oxidation number close to 0 to favor photocatalytic $1e^-$ WOR. Compared to Cu (1.90) and Ag (1.93), Au has a higher electronegativity of 2.54, close to carbon (2.55), but smaller than N (3.04). Only formation of Au–C bond is favorable for maintaining the s electron at the isolated Au site on carbon nitride because of the close electronegativity of Au and C (Supplementary Note 1). Therefore, weakening the strong interactions between Au and N to form Au–C bonds in PCN becomes the key challenge for constructing single Au atomic sites with low oxidation numbers.

Early report revealed that the oxidation state of an individual atom could be controlled by adding or removing an electron to or from the adatom using scanning tunneling microscope, resulting in an associated change of coordination configuration[22]. In this work, we carefully tuned

the coordination configuration of Au to obtain atomically dispersed Au with low oxidation state. Specifically, potassium was introduced into poly(heptazine imide) matrix to form strong K–N interactions[20]. As a result, when Au was subsequently introduced, Au could only form a bond with C on K-incorporated PCN (KPCN), leading to a notably reduced oxidation number of Au (close to 0). The results of time-dependent density function theory (TDDFT) calculation, isotopic experiments, *in-situ* spectroscopy measurements revealed that the Au on KPCN (AuKPCN) formed a trapping level for generating highly localized holes under photoexcitation. These highly localized holes could boost the $1e^-$ WOR to form highly oxidative ·OH. The $1e^-$ WOR also released the proton in the H_2O molecule, leading to notably enhanced hydrogenation during the $2e^-$ ORR (eq. 5). The photogenerated ·OH over AuKPCN greatly promoted the visible-light-response superhydrophilicity (120-fold) as compared to commercial photocatalyst. The onsite fixed-bed reactor under photo-illumination achieved a remarkable 66 L_{H2O} m^{-2} day^{-1} water disinfection rate (lg6), which is about 10 times superior than the TiO_2 photocatalytic advanced oxidation process in the most ideal case (< 4 L_{H2O} m^{-2} day^{-1}; lg4).

Results and Discussion

Photocatalytic H_2O_2 and ·OH production over AuKPCN

To block the N sites on PCN to form strong coordination with Au, KBr was used as a flux to introduce K species into the carbon nitride matrix to prepare K-incorporated PCN (KPCN)[20, 23]. Subsequently, atomically dispersed Au was anchored onto KPCN (named as AuKPCN) by a simple impregnation method using $HAuCl_4$ as the Au source (Supplementary Figure 1). Control samples including pristine PCN, KPCN, and Au on PCN (AuPCN) were also prepared as references[24]. The as-prepared AuKPCN samples could readily form stable sols, which is very promising for making AuKPCN films by drop casting or spray coating (Supplementary Figure 2).

The photocatalytic reaction to produce H_2O_2 was carried out in deionized water in the presence/absence of organic donors with different oxidative potentials to probe the reactivity of photooxidation reactions. The optimized Au content was determined to be ~0.11 wt.% in both AuPCN and AuKPCN (Supplementary Figure 3, Supplementary Table 2), and the K content in AuKPCN and KPCN maintained constant after the continuous photoreaction (Supplementary Table 3-4, Supplementary Note 2). AuKPCN exhibited an apparent quantum yield (AQY) of around 85% at the reduction side in the wavelength range of 400 to 420 nm when organic electron donors were present during the first 10 minutes of the photoreaction (Figure 1c). The similar

generation amount of H_2O_2 at the reduction site suggested that the photooxidation reaction on AuKPCN was non-selective for organic compounds with different oxidation potentials (Supplementary Table 5). To investigate the half reaction over AuKPCN at the oxidation side (eq. 3), Ag^+ and 5,5-dimethyl-1-pyrroline-N-oxide (0.2 mol L^{-1}, DMPO, scavenger for radicals) were added[17]. After the photoreaction, the reaction solution was immediately transferred for the electron spin resonance measurement. Only ·OH could be detected in the presence of AuKPCN (Figure 1d and Supplementary Figure 4) without detection of any O_2 or H_2O_2, indicating that ·OH was generated during the photocatalytic WOR on AuKPCN[17]. The AQY for ·OH generation via WOR was then investigated by co-adding Ag^+ as an electron acceptor and salicylic acid (SA) as the ·OH probe (Supplementary Note 3) in Ar atmosphere (Supplementary Table 6). The AQY of AuKPCN for ·OH generation in 10 min is close to 85%, while other reference samples (KPCN, AuPCN and PCN) show no activity. Note that the generation amount of ·OH and H_2O_2 in SA with saturated O_2 is close to 2:1 (Figure 1e), which matches well with the theoretical ratio based on $1e^-$ WOR (eq. 4) and $2e^-$ ORR (eq. 5). To the best of our knowledge, AuKPCN displayed the highest AQY reported so far for the half photocatalytic reaction to produce ·OH via $1e^-$ WOR and to produce H_2O_2 via $2e^-$ ORR (Supplementary Table 7). In a photocatalytic water disinfection and purification system based on H_2O_2, surplus photogenerated H_2O_2 could lead to severe health concerns for drinkable water. Because of the strong oxidizing capability, the photogenerated ·OH via WOR can decompose H_2O_2 if no organic species are present (eq. 6). As a result, H_2O_2 concentration (Supplementary Figure 5) was found to keep almost constant with reaction time in the reaction system having AuKPCN with different initial amounts of H_2O_2. Without organic electron donors, no H_2O_2 could be detected in the AuKPCN photocatalytic system, indicating its promising application potential for direct on-site water purification.

$$2h^+ + 2H_2O\ (l) \rightarrow 2{\cdot}OH\ (aq) + 2H^+\ (aq) \qquad (4)$$

$$2e^- + O_2\ (g) + 2H^+\ (aq) \rightarrow H_2O_2\ (aq) \qquad (5)$$

$$H_2O_2\ (aq) + 2{\cdot}OH\ (aq) \rightarrow O_2\ (g) + 2H_2O\ (l) \qquad (6)$$

Structural characterizations

To understand the superb photocatalytic performance of AuKPCN for H_2O_2 production and $1e^-$ WOR, the structures of the as-synthesized catalysts were carefully characterized. Supplementary Figures 6-7 and Figure 2a show the X-Ray diffraction patterns and high-resolution transmission

electron microscopy (HR-TEM) images, which reveal high crystallinity of the as-prepared KPCN and AuKPCN with two-dimensional (2D) sheet-like morphology[20]. The lattice fringes of 11 Å and 8.7 Å as observed in the HR-TEM image and the fast Fourier transform (FFT) can be assigned to the (110) and (100) facets of K-incorporated poly(heptazine imide) (K-PHI), respectively (Figure 2a). The electron diffraction spots of KPCN are almost identical to those of the previously reported K-PHI, which exhibits monoclinic layer symmetry[20, 25, 26]. The appearance of the 8.7 Å lattice spacing suggests that K has been successfully incorporated into the matrix of PHI to form strong interactions with the N atoms on the carbon nitride backbone (Supplementary Figure 7 and Figure 2a)[20]. As displayed in the high-angle annular dark-field scanning transmission electron microscopy (HAADF-STEM) image (Figure 2b), the isolated bright spots can be assigned to the atomically dispersed Au, which are distributed on the surface of KPCN (Figure 2b and Supplementary Figures 8-11) [27].

To investigate the interactions between the isolated Au, K species and the carbon nitride backbone, Fourier transform infrared (FTIR) and X-ray photoelectron spectroscopy (XPS) and were conducted. The FTIR spectra of KPCN and AuKPCN show typical finger prints at around 1000 cm^{-1} and 1300-1800 cm^{-1}, suggesting formation of the K-PHI like structure (Supplementary Figure 12)[19, 20]. A vibrational peak appeared at ~2140 cm^{-1}, indicating that the small amount of C≡N could be generated if K species were introduced during the synthesis. This is probably due to the formation of metal cyanamide complexes[28, 29], which is also confirmed by XPS results (Supplementary Figures 13-14) [10, 19]. The binding energy of Au 4f indicated lower oxidation numbers of Au in AuKPCN than in AuPCN (Supplementary Figures 15-17). Note that the chemical states of potassium would not be influenced by the introduction of Au species as revealed by EELS (Figures 2c-d) and XPS (Supplementary Figures 14 and 16), indicating that the K species in the carbon nitride matrix did not electronically interact with the introduced Au species[30].

To investigate the coordination environment of Au in AuKPCN, we conducted solid-state NMR (ssNMR) spectroscopy measurements of PCN, KPCN and AuKPCN. ^{13}C NMR spectrum shows that there are two distinct signals for PCN (Supplementary Figure 18). In traditional melon structure, the central carbon atom (dark diamonds in Supplementary Figure 18a) in the heptazine unit exhibits a chemical shift at 157 ppm. The signals at around 168 and 164 ppm are attributed to a peripheral carbon atom next to a NH_x (x can be 1-2) group (dark red diamonds in Supplementary Figure 18a)[31]. Note that the signals at 164 ppm and 168 ppm usually display an intensity ratio of

about 2:1, which is close to the ratio observed in melamine and melem[31]. The observed values are in good agreement with those found for sp^2-hybridized carbon atoms in other carbon nitride materials[32]. For KPCN, the central carbon atom in the heptazine unit and the peripheral carbon atom next to an imide (NH) group exhibit similar chemical shifts at 157 ppm and around 164-168 ppm, respectively. The ^{13}C NMR signal at 172 ppm arises from the carbon atom next to a deprotonated imide bridge (green and gold diamonds in Supplementary Figure 19a). This bridge C is only connected to nitrogen with a chemical shift at 210 ppm corrected by glycine (Supplementary Figure 19d), a typical value for non-protonated nitrogen[20]. When Au atoms are loaded onto the framework of KPCN to form AuKPCN, the intensity of C at the chemical shift of 172 ppm significantly weakened (Supplementary Figure 20). Notably, a new distinct chemical shift at 111 ppm emerged, which is at the chemical shift of sp^2 carbon and sp^3 carbon.

To further investigate whether the chemical shift at 111 ppm was originated from the interaction between Au and C, we carefully conducted the structure optimization based on density functional theory (DFT) by putting one Au atom on the model of K-PHI (Supplementary Figure 20) as a starting model. The ^{13}C NMR spectra of these optimized models were simulated by the function of B97D at def2TZVPP level, and all chemical shifts in NMR spectra were corrected by applying trimethyl silane (TMS) calculated using the GIAO method (B3LYP/6-311+G(2d, p)). The simulated NMR spectrum of melon showed two groups of distinguished chemical shift at 162-158 ppm and 156-153 ppm, corresponding to central carbon atoms and peripheral carbon atoms next to NH_x (x = 1-2). Negligible changes in the simulated NMR spectrum of K-PHI were noticed. The slight chemical shift could be attributed to more negative charges of C atoms after replacing H with K. Notably, two chemical shifts at 166.5 ppm and 165.1 ppm clearly appeared, corresponding to carbon atoms next to a deprotonated imide bridge. This is consistent with the experimental ss-NMR result. When Au was introduced into the K-PHI model, the two chemical shifts at 166.5 ppm and 165.1 ppm completely disappeared, which is also consistent with the significantly decreased signal at 172 ppm as shown in Supplementary Figure 19c. Notably, several new chemical shifts in the range between 150 ppm and 100 ppm appeared. This could be attributed to the C atom next to Au atom, which shifted from 165.1 ppm to 120 ppm in the simulated NMR spectrum, consistent with the shift from 172 ppm to 111 ppm in the experimental ss-NMR spectrum. The chemical environment of N atoms in PCN, KPCN and AuKPCN was also studied by ^{15}N NMR spectroscopy

(Supplementary Note 4), which further support the formation of strong interaction between Au and C.

To further differentiate the Au coordination structure in AuKPCN and AuPCN, we performed X-ray absorption near edge structure (XANES, Figures 2d-e) of C 1s and N 1s. When Au was loaded onto PCN/KPCN, the signal for C 1s to π^* transition significantly increased. On the other hand, the signal for C 1s to δ^* transition was found significantly increased only in AuKPCN, but not in AuPCN (Figure 2d)[33-35]. The intensities of the N 1s to δ^* and N 1s to π^* transitions kept nearly the same when Au was introduced onto KPCN, while decreased when Au was introduced onto PCN[33-35] (Figure 2e). The changing tendency of chemical states of N and C atoms further suggests their different coordination status with Au in the two samples. As revealed by ss-NMR, Mayer bond order[36], bond angle analysis and electron localization analysis, the main interaction between Au and C is mainly contributed by the overlapping of 6s orbitals of Au and 2p orbitals of hybridized sp^2 C and N (Supplementary Figures 21-24, Supplementary Note 5). The density of electron cloud of C (52) is slightly lower than that of the other neighboring C atoms (53 and 47), again revealing that the hybridization property of C (52) is between that of a typical sp^2 C (e.g., C (75)) and a sp^3 C (Supplementary Tables 8-9).

The oxidation state of the Au atoms in AuKPCN was then determined by XANES at the Au L_3-edge. As compared in Figure 2f, the white-line intensity of AuKPCN is much lower than that of AuPCN, indicating notably lower oxidation state of Au in AuKPCN. Using Au foil, AuCl and $HAuCl_4$ as the references, the valence state of Au was estimated to be around +0.7 in AuKPCN and +1.9 in AuPCN, which is consistent with the XPS results (Supplementary Note 6). FT-EXAFS spectra obtained from the k^3-weighted K-space (Supplementary Figure 25) of AuKPCN and AuPCN display only one peak at ~1.62 Å with no Au-Au interaction at 2.30 Å, implying that the Au in AuKPCN and AuPCN are atomically dispersed. To further identify the Au coordination structures, models of carbon nitride with single Au sites on PCN (Melon_Au) and on KPCN (AuK-PHI)[18, 37, 38] were simulated by DFT (Supplementary Figure 21). Based on all possible predicted structure models, the best fitting results for the first shell of the EXAFS spectra[39] (Figure 2g, Supplementary Figure 26 and Supplementary Table 10) support the distinct coordination structure of AuPCN and AuKPCN. The fitting result of AuPCN shows that each Au atom is coordinated with 2.9 N atoms in average and can be well fitted by the Melon_Au[10]. The small coordination number of 2.5 C/N for Au also consistent with model of AuK-PHI. Therefore, the oxidation state

of atomically dispersed Au decreased from +1.9 in AuPCN to around +0.7 in AuKPCN, which supported the formation of strong interaction between Au and C (Supplementary Figure 27). Although we cannot obtain a clear microscopy image for identifying "*the C–N six-membered ring as well as Au atoms on the substrate"* because of the beam-sensitivity of poly(heptazine imides) (Supplementary Note 7), the spectroscopy (ss-NMR, XAFS, XPS, etc.) and simulation results do indicate there exist strong interactions between Au and C in AuKPCN, facilitated by overlap of the 6s orbital of Au and the 2p orbital of C.

Photo-physiochemical properties of AuKPCN

The optical properties of PCN, KPCN, AuPCN and AuKPCN were then carefully investigated to clarify the function of Au species with low oxidation numbers for $1e^-$ photocatalytic WOR. The estimated band structure indicated sufficient thermodynamic driving force for both $2e^-$ ORR and $1e^-$ WOR in aqueous solution under photoexcitation (Supplementary Figures 28-31). Additionally, transient absorption spectroscopy measurements suggested that the water oxidation reaction was boosted by photogenerated holes on AuKPCN, which simultaneously accelerated the $2e^-$ ORR on the melem sites (Supplementary Figure 32, Figure 3a, Supplementary Note 8). To give a comprehensive view of the electronic configuration, we used the optimized structure model to investigate whether the Au sites with different oxidation states could influence the excitation properties. The density functional theory (DFT) simulation results show that if electrons of 6s orbital remain in the AuKPCN matrix (AuK-PHI model), the valence electrons of Au will shift to form several new electronic states higher than the energetic levels of C 1s and N 1s (Figures 3b-c). On the contrary, the partial DOS (PDOS) of AuPCN (Melon_Au) shows that the molecular orbital (MO) of the 5d Au is mainly located at a lower energy than the energy of N 2p (Supplementary Figure 33) [40]. These results indicate that the valence electrons of Au with low oxidation states can participate in the photooxidation reaction. The excitation properties obtained by time dependent DFT (TDDFT) (Supplementary Figures 34-36) also revealed that the transitions form a typical s-orbital spherical (Figure 3b, Supplementary Tables 11-14) isosurface, highlighting the remarkable effect of low-valent Au on the oxidation process (Supplementary Note 8)[41, 42]. To quantitatively determine whether the introduced Au species could participate in the photooxidation reaction, we defined a weighted arithmetic electron-hole distance (WD) index by normalizing the oscillator strength (Supplementary Note 9) to simultaneously describe charge concentration and separation (Supplementary Figures 37-39). We summed the values of WD index at 50 excited

states at the Au sites. The value of models for representing AuKPCN is about 3 times larger than that for AuPCN (Figure 3d), indicating that highly oxidative holes can be formed at the Au sites on AuKPCN during photoexcitation. To further confirm the role of Au on KPCN during photoexcitation, *in-situ* XPS measurements were performed (Figures 3e and Supplementary Figure 40). The binding energy of Au 4f for AuKPCN displays a notable shift accompanying with light on and off. On the contrary, there is almost no binding energy change of Au 4f for AuPCN. These results further corroborate that the Au sites with low oxidation states on KPCN could help to generate highly concentrated holes during light irradiation.

Photocatalytic mechanism and applications of AuKPCN

To probe the photocatalytic mechanism, *in-situ* FTIR measurements were carried out, and the results are shown in Supplementary Figures 41-43. It is found that the signal of water adsorption is extremely weak over PCN, KPCN and AuPCN, consistent with the poor photocatalytic activity of these samples. For the spectrum recorded over AuKPCN, the water vibrational peak at around 1600 cm^{-1} can be clearly observed, indicating that the reaction of water oxidation has been significantly boosted by introducing Au species onto KPCN (Figure 4a)[43, 44]. To further investigate how water influenced the photocatalytic oxidation reaction, an isotope experiment using H_2O^{18} as the reactant was conducted (Supplementary Figure 43). The stretching vibration of $C=O^{18}$ and the bending vibration of $C–O^{18}H$ showed obvious wavenumber shifts compared with that of $C=O^{16}$ and $C–O^{16}H$, while almost no shift of stretching and bending vibration of C–C were detected. These results are well consistent with the simulation results, indicating that the O in H_2O did participate in the photocatalytic oxidation reaction (Supplementary Figure 44). Combining with the results from ESR measurements (Figure 1d), the introduction of Au species on KPCN was found to boost the ·OH generation via the $1e^-$ photocatalytic WOR. This $1e^-$ photocatalytic WOR could produce ·OH and unleash proton by chemically activating water, and subsequently the produced proton would diffuse to the neighboring melem sites to accelerate ORR (Supplementary Note 10) based on the results of isotopic experiments[45] (Figures 4c-f and Supplementary Figure 45) and Raman spectroscopy (Figure 4g) [46, 47].

The stability of PCN-based materials against exposure to ·OH is a significant concern. The influence of ambient dissolved oxygen and organic electron donor on the stability of AuKPCN were carefully investigated to reveal the oxidation pathway of ·OH in semi-realistic conditions (Supplementary Table 15). The ·OH generated over AuKPCN can react with the added organic

electron donor, the produced H_2O_2 or AuKPCN itself (characterized by NO_3^- formation in solution and N_2 formation in the gas phase). If the photoreaction was performed in Ar atmosphere with added electron acceptor Ag^+, the generated ·OH would react with AuKPCN that could decompose AuKPCN to release NO_3^- and N_2. In experiments without artificial O_2 supply (e.g., water treatment applications), the changes of ambient dissolved oxygen (from 8 mg L^{-1} to 2 mg L^{-1}) as well as variation of organic concentration show no obvious influence on the stability of AuKPCN, i.e., no NO_3^- or N_2 could be detected after the photoreaction. Therefore, ambient dissolved oxygen in water is crucial to generate sufficient amount of H_2O_2 to keep AuKPCN stable during practical water disinfection and treatment process as water becomes purified. Consequently, we developed a 3-phase water disinfection device (Figure 5a, Supplementary Figure 46), using photocatalytic sheets prepared by polytetrafluoroethylene (PTFE) coated with AuKPCN (Figure 5a, left) to supply sufficient O_2 at the interface between AuKPCN and water (the concentration of dissolved oxygen in the bulk solution was determined to be around 5 mg L^{-1} during the disinfection process). With O_2 supplement through the PTFE membrane, ·OH generated via water oxidation preferentially oxidized organics, bacteria (0.16~1.14 V vs. NHE, with organics) or H_2O_2 (1.44 V vs. NHE, without organics), rather than the KPCN framework (>1.81 V vs. NHE, the redox potential of VBM) (Figures 5b-d, Supplementary Table 15). The as-developed water disinfection/treatment device maintained almost constant performance in 50 continuous testing cycles over 25 h (Figure 5e). It is noteworthy that post-characterizations of AuKPCN after continuous photoreaction for 5 days in pure water under ambient condition (dissolved oxygen: about 5 mg L^{-1}) show almost the same structure as the fresh sample (Supplementary Figures 47-48), indicating excellent photocatalytic stability of AuKPCN. OA and *p*-hydroxybenzoic acid (PHBA) could be decomposed in 20 mins and 30 mins, respectively, under visible light illumination, together with a $-\log_{10}(C/C_0) = 6$ photocatalytic disinfection (*E. coli*) rate in 10 min (Supplementary Figure 49). The photocatalytic activity of AuKPCN is higher than P25 even in the UV region (Supplementary Figure 50). These efficiencies are far better than those achieved over commercial photocatalysts and are even comparable with those of the photocatalytic ozone treatment systems (Figure 5f, Supplementary Tables 16-17, Supplementary Notes 11)[48]. The water disinfection bags are portable and can be used in extreme conditions for drinkable water acquisition. Contaminated water can be simply poured into the bags, and pathogens will be killed by photogenerated ·OH, which can meet the standards of drinkable water (Drinking Water Quality Standards in Japan and China).

The simultaneous generation of H_2O_2 and ·OH also offers AuKPCN with excellent visible-light-response super-hydrophilicity (Figure 5g). Under visible light illumination ($\lambda \geqslant 420$ nm, weak room light, about 1 mW cm^{-2}), the water contact angle of the AuKPCN film decreased to approximately 4° within 1 second. This is about 120 times faster than the response speed of iron-loaded rutile titanium dioxide nanorods[49] (a commercial visible-light-responsive self-cleaning spray developed by Dr. Ohno), which took about 120 seconds to reach the water contact angle of around 10° (Supplementary Figure 51). The presence of photogenerated ·OH on AuKPCN resulted in a more than 120-fold enhancement in efficiency for visible-light-response super-hydrophilicity compared to that of commercial TiO_2. The as-prepared AuKPCN nano-coating could be applied in various substrates including plastics, foams, steels, etc (Supplementary Figures 52-53).

Conclusions

In summary, AuKPCN has been successfully designed and constructed by a facile impregnation method, which exhibits significantly boosted $1e^-$ photocatalytic water oxidation and $2e^-$ photocatalytic oxygen reduction activities for simultaneously generating ·OH and H_2O_2 with AQE over 85% in the wavelength region from 400 to 420 nm. The atomically dispersed Au with low oxidation number could append its 6s orbital into the band diagram of AuKPCN that formed a trapping level for generating highly localized holes under photoexcitation. These highly localized holes could boost the $1e^-$ water oxidation reaction to form highly oxidative ·OH and at the same time unbind the proton in the H_2O molecule, leading to notably enhanced hydrogenation during the $2e^-$ ORR. The photogenerated ·OH over AuKPCN could quickly degrade refractory organic pollutants in water and lead to an over 120-fold efficiency enhancement for visible-light-response super hydrophilicity compared to commercial photocatalyst. The onsite fixed-bed reactor designed based on AuKPCN achieved a remarkable 66 L m^{-2} d^{-1} disinfection rate (lg6), 1 order of magnitude superior than TiO_2 based on the most ideal case (< 4 L m^{-2} d^{-1}; lg4).

Acknowledgements

The authors acknowledge the financial support of City University of Kong Hong startup fund (9020003, B.L.), ITF–RTH - Global STEM Professorship (9446006, B.L.), Mitsubishi Chemical Corporation, JSPS Grant-in-Aid for Scientific Research (B, No. 20H02847, T.O.), The National Key Research and Development Program of China (2021YFA1600800, C.S.), Grant-in-Aid for JSPS Fellows (DC2, 20J13064), Project National Natural Science Foundation of China (22372102,

C.S.; 21805191, Q.Z.; 21972094 C.S.), the Guangdong Basic and Applied Basic Research Foundation (2024A1515010976, 2020A1515010982), Shenzhen Science and Technology Program (RCJC20200714114434086, C.S.), and Shenzhen Peacock Plan (202108022524B, Q.Z.). Research Team Cultivation Program of Shenzhen University (2023QNT013, C.S.). The authors thank Dr. Jiadong Xiao, Dr. Takashi Hisatomi, Prof. Kazunari Domen from Shinshu University for their help in ·OH detection and D_2O experiments. The authors also thank Dr. Xiangbin Cai (Nanyang Technological University), Dr. Cailing Chen (King Abdullah University of Science and Technology), Dr. Yu Han (King Abdullah University of Science and Technology), Dr. Lin Gu (Institute of Physics, Chinese Academy of Sciences), Dr. Ruichun Luo (University of Chinese Academy of Sciences), Dr. Xingjie Peng (University of Chinese Academy of Sciences), Dr. Wu Zhou (University of Chinese Academy of Sciences), Miss Kangdi Niu (Southern University of Science and Technology), Dr. Wu Wang (Southern University of Science and Technology), Dr. Junhao Lin (Southern University of Science and Technology) and Dr. Nan Jian (Electron Microscope Center of the Shenzhen University), for their help in HR-TEM measurements. The authors thank Dr. Xusheng Zheng (National Synchrotron Radiation Laboratory, University of Science and Technology of China) for his help in analyzing data of soft X-ray absorption.

Author Contributions Statement

Z.T., T.O. and B.L. conceptualized the project. T.O., C.S. and B.L. supervised the project. Z.T. synthesized the catalysts, conducted the catalytic tests and the related data processing, and performed materials characterization and analysis with the help of H.Y., W.C., Q.Z., Y.-R.L., T.-S.C., S.L. and J.D. K.K. and A.Y. conducted transient absorption spectroscopy measurements. C.W., Z.Z., P.C. and Z.T. designed and prepared the practical devices for solar water disinfection. S.H. and Z.T. prepared the self-cleaning nanocoating. Z.T. performed the theoretical study. Z.T. and B.L. wrote the manuscript with support from all authors.

Competing Interests Statement

The authors declare no competing interests.

Figure 1 | Photocatalytic ·OH and H_2O_2 production over AuKPCN. a, Schematic diagram showing the intermediates in the multielectron-transfer processes of WOR. The most efficient reaction for ·OH generation is the $1e^-$ WOR, which is theoretically two-times efficient of the ·OH

generation from $2e^-$ WOR. **b**, Excited properties of group 11 elements at different chemical states. Left: The metallic sites are at high oxidation numbers. The valence electron of s orbital can be extracted by the neighboring atoms of high electronegativity. The valence electron of s orbital will not participate in the reaction. Right: The metallic sites are at low oxidation numbers (close to 0). The valence electron of s orbital can remain confined at the isolated metallic site, forming a highly concentrated hole during photoexcitation. **c,** Average apparent quantum yield (AQY) of AuKPCN for photocatalytic H_2O_2 production at 420 nm in organic electron donors of ethanol (Et-OH), oxalic acid (OA), *p*-hydroxybenzoic acid (PHBA), t-butanol, salicylic acid (SA), or terephthalic acid (TA) in 10 min. **d**, ESR spectra of AuKPCN recorded in 0.1 M $AgNO_3$ solution saturated with Ar using 5,5-diemthyl-1-pyrroline N-oxide (DMPO) as the radical trapper. **e**, Generation amount of ·OH and H_2O_2 in SA with saturated O_2. Irradiation condition for **c** and **e**: $\lambda = 420$ nm (Xe lamp with a band-pass filter with the light intensity of 20 W m^{-2}) at 298 K. Irradiation condition for **d**: $\lambda \geq 420$ nm (Xe lamp, light intensity at 420-500 nm: 30.3 W m^{-2}) at 298 K.

Figure 2 | Structural characterization of AuKPCN. a, High-resolution transmission electron microscopy image of AuKPCN. Inset shows the FFT pattern. **b**, High-magnification HAADF-STEM image of AuKPCN. Inset shows the size distribution of the bright spots. The estimated size distribution shows that about 99.6% of the Au species are less than 0.2 nm, demonstrating that Au exists exclusively as isolated single atoms. **c**, Electron energy loss spectroscopy spectra of KPCN and AuKPCN. **d-e**, Normalized carbon (d) and nitrogen (e) K-edge X-ray absorption near edge structure (XANES) spectra of PCN, KPCN, AuPCN and AuKPCN. Inset shows the enlarged spectra for representing transitions of C 1s to δ^* (d) and N 1s to π^* (e). **f**, Au L_3-edge XANES spectra of Au foil, $HAuCl_4 \cdot nH_2O$, AuPCN and AuKPCN. Inset shows the estimation of the oxidation number of Au by using white line intensity. **g**, Fitting of the EXAFS spectra for AuKPCN based on the model obtained from density functional theory (DFT) optimization (inset).

Figure 3 | Excitation properties of AuKPCN. a, Comparison of transient absorption decay among film samples of PCN, AuPCN, KPCN and AuKPCN at 5000 cm^{-1} under N_2, O_2 and H_2O atmosphere (details for the pulse light: 420 nm, 6 ns, 5 mJ and 0.2 Hz, the atmosphere pressure of N_2, O_2 and H_2O were set at 20 Torr). The absorption intensity at the time point of 1 ms was used as the benchmark for investigating how deeply trapped electrons/holes interact with N_2, O_2 and H_2O. **b**, Total density of states (TDOS), partial density of states (PDOS) and overlapped density

of states (ODOS) of AuK-PHI model. **c**, Isosurface (Green and blue regions) of the highest occupied molecular orbital (MO325) of AuK-PHI model. **d**, Weighted arithmetic hole distance (WD) index calculated for Au sites on Au_melon model and AuK-PHI model. **e**, *In-situ* high resolution Au 4f XPS spectra of AuPCN (left) and AuKPCN (right) under light irradiation.

Figure 4 | Photocatalytic water oxidation and oxygen reduction on AuKPCN. a, *In-situ* FTIR spectra of PCN, AuPCN, KPCN and AuKPCN exposed to humid $O^{16}{}_2$ ($CH_3CH_2O^{16}H$ (10% v/v) aqueous solution was used for supplying the humid atmosphere of ethanol and H_2O) under light irradiation for 30 mins. **b**, Isotopic experiment of water oxidation in humid $O^{16}{}_2$ and H_2O^{18} for investigating the water oxidation mechanism. The other conditions are the same as those in **a**. **c-f**, Isotopic experiment to investigate mass transfer of proton in the system of AuKPCN (c), AuPCN (d), PCN (e) and KPCN (f) during the photocatalytic H_2O_2 production in D_2O or H_2O with addition of Et-OH (10% v/v). **g**, Raman spectra recorded during photoreaction in a Et-OH (10% v/v) aqueous solution with saturated oxygen. Over PCN, KPCN and AuPCN, a vibration band appears at around 900 cm^{-1}, which can be assigned to the C−O vibration and O−O stretching on the melem[8]. While over AuKPCN, besides the 900 cm^{-1} vibration, a new absorption band at 859 cm^{-1} develops with irradiation time, which can be assigned to the O–O stretching of μ-peroxide (–OOH) species with end-on adsorption configuration[46, 47].

Figure 5 | Photocatalytic mechanism and stability of AuKPCN for water purification and disinfection. a, Schematic diagram showing photocatalytic H_2O_2 and ·OH production over 3-phase AuKPCN coated polytetrafluoroethylene (PTFE) sheets. **b**, Redox potentials of typical refractory organics, bacteria, H_2O_2 and ·OH (on surface and in aqueous solution). **c-d**, Preferential oxidation pathways in aqueous solution with (c) or without (d) the existence of refractory organics or bacteria. The ·OH (aq.) has the highest oxidation potential of 2.38 V vs. NHE. **e**, Long-term stability (25 h, 50 cycles) of the as-developed AuKPCN device for solar water disinfection. *E. coli* (10^6 cfu mL^{-1}) was used as a stock solution. After every 0.5 h disinfection process, water was poured out, and the bag was washed by deionized water. Then, the biocontaminated water containing *E. coli.* was immediately poured into the bag. The highest water depth in the bag was controlled to be 5 mm. **f**, Comparison of log disinfection performance (disinfection efficiency and disinfection capability) of AuKPCN sheet with the efficiency of other photocatalysts and traditional techniques: this work, AM 1.5 sunlight, 100 mL), FLV-MoS_2/Cu (AM 1.5 sunlight, 25

mL)[50], Ag/TiO_2 (100 mL, UVB 2 W m^{-2})[51], F-g-C_3N_4-30-EP (50 mL, 1000 W m^{-2}, >400 nm)[52], TiO_2/PS (UVB: 365 nm 1 mW cm^{-2})[53], TiO_2/cellulose 6 (UVB: 365 nm 20 mW cm^{-2})[54], MoS_2 co-catalytic Fe^{2+}/H_2O_2 (100 mL, no light, 2 mg mL^{-1})[55], $FeSO_4/H_2O_2$ (230 mL, 1200 W m^{-2})[56], and UV/ClO_2 (no catalyst)[57]. **g**, Self-cleaning coating on 5160 steel surfaces: PCN, AuPCN, KPCN and AuKPCN (with superhydrophilicity under room light irradiation).

References

1. Zhang, J., Mück-Lichtenfeld, C. & Studer, A. Photocatalytic phosphine-mediated water activation for radical hydrogenation. *Nature* **619**, 506-513 (2023).
2. Gligorovski, S., Strekowski, R., Barbati, S. & Vione, D. Environmental implications of hydroxyl radicals (·OH). *Chem. Rev.* **115**, 13051-13092 (2015).
3. (IMISDG6), U.-W.I.M.I.f.S. (UN-Water, Geneva, Switzerland; 2021).
4. Donde, O.O., Atoni, E., Muia, A.W. & Yillia, P.T. COVID-19 pandemic: Water, sanitation and hygiene (WASH) as a critical control measure remains a major challenge in low-income countries. *Water Res.* **191**, 116793 (2021).
5. Loeb, S.K. et al. The technology horizon for photocatalytic water treatment: Sunrise or sunset? *Environ. Sci. Technol.* **53**, 2937-2947 (2019).
6. Jeon, I., Ryberg, E.C., Alvarez, P.J.J. & Kim, J.-H. Technology assessment of solar disinfection for drinking water treatment. *Nat. Sustain.* **5**, 801-808 (2022).
7. Hou, H., Zeng, X. & Zhang, X. Production of hydrogen peroxide by photocatalytic processes. *Angew. Chem. Int. Ed.* **59**, 17356-17376 (2020).
8. Shiraishi, Y. et al. Sunlight-driven hydrogen peroxide production from water and molecular oxygen by metal-free photocatalysts. *Angew. Chem. Int. Ed.* **53**, 13454-13459 (2014).
9. Kim, H. et al. Spontaneous generation of H_2O_2 and hydroxyl radical through O_2 reduction on copper phosphide under ambient aqueous condition. *Environ. Sci. Technol.* **53**, 2918-2925 (2019).
10. Teng, Z. et al. Atomically dispersed antimony on carbon nitride for the artificial photosynthesis of hydrogen peroxide. *Nat. Catal.* **4**, 374-384 (2021).
11. Shiraishi, Y. et al. Resorcinol–formaldehyde resins as metal-free semiconductor photocatalysts for solar-to-hydrogen peroxide energy conversion. *Nat. Mater.* **18**, 985-993 (2019).
12. Parvulescu, V.I., Epron, F., Garcia, H. & Granger, P. Recent progress and prospects in catalytic water treatment. *Chem. Rev.* **122**, 2981-3121 (2022).
13. Rahim Pouran, S., Abdul Aziz, A.R. & Wan Daud, W.M.A. Review on the main advances in photo-Fenton oxidation system for recalcitrant wastewaters. *J. Ind. Eng. Chem.* **21**, 53-69 (2015).
14. Shi, X., Back, S., Gill, T.M., Siahrostami, S. & Zheng, X. Electrochemical synthesis of H_2O_2 by two-electron water oxidation reaction. *Chem* **7**, 38-63 (2021).
15. Nosaka, Y. & Nosaka, A.Y. Generation and detection of reactive oxygen species in photocatalysis. *Chem. Rev.* **117**, 11302-11336 (2017).
16. Kou, M. et al. Molecularly engineered covalent organic frameworks for hydrogen peroxide photosynthesis. *Angew. Chem. Int. Ed.* **61**, e202200413 (2022).

17. Wang, Q. & Domen, K. Particulate photocatalysts for light-driven water splitting: mechanisms, challenges, and design strategies. *Chem. Rev.* **120**, 919-985 (2020).
18. Banerjee, T., Podjaski, F., Kröger, J., Biswal, B.P. & Lotsch, B.V. Polymer photocatalysts for solar-to-chemical energy conversion. *Nat. Rev. Mater.* **6**, 168-190 (2021).
19. Lau, V.W.-h. et al. Rational design of carbon nitride photocatalysts by identification of cyanamide defects as catalytically relevant sites. *Nat. Commun.* **7**, 12165 (2016).
20. Schlomberg, H. et al. Structural Insights into poly(heptazine imides): A light-storing carbon nitride material for dark photocatalysis. *Chem. Mater.* **31**, 7478-7486 (2019).
21. Chen, R. et al. Spatiotemporal imaging of charge transfer in photocatalyst particles. *Nature* **610**, 296-301 (2022).
22. Repp, J., Meyer, G., Olsson, F.E. & Persson, M. Controlling the charge state of individual gold adatoms. *Science* **305**, 493-495 (2004).
23. Savateev, A., Pronkin, S., Willinger, M.G., Antonietti, M. & Dontsova, D. Towards organic zeolites and inclusion catalysts: Heptazine imide salts can exchange metal cations in the solid state. *Chem. Asian J.* **12**, 1517-1522 (2017).
24. Wang, X. et al. A metal-free polymeric photocatalyst for hydrogen production from water under visible light. *Nat. Mater.* **8**, 76-80 (2009).
25. Mesch, M.B. et al. Solving the hydrogen and lithium substructure of poly(triazine imide)/LiCl using NMR crystallography. *Chem. Eur. J.* **22**, 16878-16890 (2016).
26. Wirnhier, E. et al. Poly(triazine imide) with intercalation of lithium and chloride ions $[(C_3N_3)2(NH_xLi_{1-x})_3 \cdot LiCl]$: A crystalline 2D carbon nitride network. *Chem. Eur. J.* **17**, 3213-3221 (2011).
27. Gao, C. et al. Heterogeneous single-atom photocatalysts: Fundamentals and applications. *Chem. Rev.* **120**, 12175-12216 (2020).
28. Schwarzer, A., Saplinova, T. & Kroke, E. Tri-s-triazines (s-heptazines)—From a "mystery molecule" to industrially relevant carbon nitride materials. *Coord. Chem. Rev.* **257**, 2032-2062 (2013).
29. Makowski, S.J., Schwarze, A., Schmidt, P.J. & Schnick, W. Rare-earth melonates $LnC_6N_7(NCN)_3 \cdot xH_2O$ (Ln = La, Ce, Pr, Nd, Sm, Eu, Tb; x = 8–12): Synthesis, crystal structures, thermal behavior, and photoluminescence properties of heptazine salts with trivalent cations. *Eur. J. Inorg. Chem.* **2012**, 1832-1839 (2012).
30. Wu, C. et al. Polarization engineering of covalent triazine frameworks for highly efficient photosynthesis of hydrogen peroxide from molecular oxygen and water. *Adv. Mater.* **34**, 2110266 (2022).
31. Jürgens, B. et al. Melem (2,5,8-Triamino-tri-s-triazine), an important intermediate during condensation of melamine rings to graphitic carbon nitride: Synthesis, structure determination by X-ray powder diffractometry, solid-state NMR, and theoretical studies. *J. Am. Chem. Soc.* **125**, 10288-10300 (2003).
32. Damodaran, K., Sanjayan, G.J., Rajamohanan, P.R., Ganapathy, S. & Ganesh, K.N. Solid state NMR of a molecular self-assembly: Multinuclear approach to the cyanuric acid-melamine system. *Org. Lett.* **3**, 1921-1924 (2001).
33. Lee, J.H. et al. Carbon dioxide mediated, reversible chemical hydrogen storage using a Pd nanocatalyst supported on mesoporous graphitic carbon nitride. *J. Mater. Chem. A* **2**, 9490-9495 (2014).

34. Wang, W. et al. Potassium-Ion-assisted regeneration of active cyano groups in carbon nitride nanoribbons: Visible-light-driven photocatalytic nitrogen reduction. *Angew. Chem. Int. Ed.* **58**, 16644-16650 (2019).
35. Zhang, J.-R. et al. Accurate K-edge X-ray photoelectron and absorption spectra of g-C_3N_4 nanosheets by first-principles simulations and reinterpretations. *Phys. Chem. Chem. Phys.* **21**, 22819-22830 (2019).
36. Bridgeman, A.J., Cavigliasso, G., Ireland, L.R. & Rothery, J. The Mayer bond order as a tool in inorganic chemistry *J. Chem. Soc., Dalton Trans.*, 2095-2108 (2001).
37. Kessler, F.K. et al. Functional carbon nitride materials — design strategies for electrochemical devices. *Nat. Rev. Mater.* **2**, 17030 (2017).
38. Lin, L., Yu, Z. & Wang, X. Crystalline carbon nitride semiconductors for photocatalytic water splitting. *Angew. Chem. Int. Ed.* **58**, 6164-6175 (2019).
39. Ravel, B. & Newville, M. ATHENA, ARTEMIS, HEPHAESTUS: data analysis for X-ray absorption spectroscopy using IFEFFIT. *J. Synchrotron Radiat.* **12**, 537-541 (2005).
40. Lin, L. et al. Molecular-level insights on the reactive facet of carbon nitride single crystals photocatalysing overall water splitting. *Nat. Catal.* **3**, 649-655 (2020).
41. Lu, T. & Chen, F. Multiwfn: A multifunctional wavefunction analyzer. *J. Comput. Chem.* **33**, 580-592 (2012).
42. Bredas, J.-L. Mind the gap! *Mater. Horiz.* **1**, 17-19 (2014).
43. Ye, J.-Y., Jiang, Y.-X., Sheng, T. & Sun, S.-G. In-situ FTIR spectroscopic studies of electrocatalytic reactions and processes. *Nano Energy* **29**, 414-427 (2016).
44. Beyhan, S., Uosaki, K., Feliu, J.M. & Herrero, E. Electrochemical and in situ FTIR studies of ethanol adsorption and oxidation on gold single crystal electrodes in alkaline media. *J. Electroanal. Chem.* **707**, 89-94 (2013).
45. Hisatomi, T., Maeda, K., Takanabe, K., Kubota, J. & Domen, K. Aspects of the water splitting mechanism on $(Ga_{1-x}Zn_x)(N_{1-x}O_x)$ photocatalyst modified with $Rh_{2-y}CryO_3$ Cocatalyst. *J. Phys. Chem. C* **113**, 21458-21466 (2009).
46. Jones, R.D., Summerville, D.A. & Basolo, F. Synthetic oxygen carriers related to biological systems. *Chem. Rev.* **79**, 139-179 (1979).
47. Nakamura, R. & Nakato, Y. Primary intermediates of oxygen photoevolution reaction on TiO_2 (Rutile) particles, revealed by in situ ftir absorption and photoluminescence measurements. *J. Am. Chem. Soc.* **126**, 1290-1298 (2004).
48. Xiao, J., Xie, Y., Rabeah, J., Brückner, A. & Cao, H. Visible-light photocatalytic ozonation using graphitic C_3N_4 catalysts: A hydroxyl radical manufacturer for wastewater treatment. *Acc. Chem. Res.* **53**, 1024-1033 (2020).
49. Murakami, N., Ono, A., Nakamura, M., Tsubota, T. & Ohno, T. Development of a visible-light-responsive rutile rod by site-selective modification of iron(III) ion on {111} exposed crystal faces. *Appl. Catal. B* **97**, 115-119 (2010).
50. Liu, C. et al. Rapid water disinfection using vertically aligned MoS_2 nanofilms and visible light. *Nat. Nanotechnol.* **11**, 1098-1104 (2016).
51. Sontakke, S., Modak, J. & Madras, G. Effect of inorganic ions, H_2O_2 and pH on the photocatalytic inactivation of Escherichia coli with silver impregnated combustion synthesized TiO_2 catalyst. *Appl. Catal. B: Environ.* **106**, 453-459 (2011).
52. Teng, Z. et al. Edge-Functionalized g-C_3N_4 Nanosheets as a Highly Efficient Metal-free Photocatalyst for Safe Drinking Water. *Chem* **5**, 664-680 (2019).

53. Varnagiris, S. et al. Floating TiO_2 photocatalyst for efficient inactivation of *E. coli* and decomposition of methylene blue solution. *Sci. Total Environ.* **720**, 137600 (2020).
54. De Vietro, N. et al. Photocatalytic inactivation of *Escherichia coli* bacteria in water using low pressure plasma deposited TiO_2 cellulose fabric. *Photochem. Photobiol. Sci.* **18**, 2248-2258 (2019).
55. Liu, J. et al. Molybdenum sulfide Co-catalytic Fenton reaction for rapid and efficient inactivation of *Escherichia coli*. *Water Res.* **145**, 312-320 (2018).
56. Giannakis, S. et al. Ultrasound enhancement of near-neutral photo-Fenton for effective *E. coli* inactivation in wastewater. *Ultrason. Sonochem.* **22**, 515-526 (2015).
57. Murphy, H.M., Payne, S.J. & Gagnon, G.A. Sequential UV- and chlorine-based disinfection to mitigate *Escherichia coli* in drinking water biofilms. *Water Res.* **42**, 2083-2092 (2008).

Methods

Preparation of photocatalysts

Unless otherwise stated, the purities of all reagents for photocatalysts preparation and for photoelectrochemical measurements are above the analytical grade. The pristine PCN was prepared according to the reported method[1]. In a typical synthesis of KPCN, 5.95 g of potassium bromide was added into the synthesis. Being specific, melamine (4.0 g, Alfa Aesar) was ground with KBr (5.95 g, Alfa Aesar) in 3 mL ethanol and 1 mL glycol in an agate mortar for 1 h. After drying at 65 °C, the resultant mixture was heated to 560 °C for 4 h at a ramping rate of 2.2 °C min^{-1} in a tube furnace (inner diameter: 4 cm) in N_2 atmosphere (50 mL min^{-1}). After cooled to room temperature, the bright yellow-green product was ball milled (400 rpm, 3 h) with ZrO_2 balls of Φ~0.4 mm in ethanol. The sample was washed by boiling deionized water several times, collected by filtration, and dried at 60 °C in a vacuum oven for 12 h.

The AuPCN and AuKPCN were prepared by a chemical deposition method as follows: a certain amount of PCN or KPCN was dispersed in 26 mL water under sonication for 60 min at 60 °C, followed by adding a certain amount of $HAuCl_4$. The mixture was then bubbled with N_2 for 30 min (100 mL min^{-1}). The reaction system was carefully sealed, and then heated to 60 °C for 8 h. After cooling down to room temperature, the sample was washed by deionized water and ethanol several times, collected by filtration, and dried at 60 °C in a vacuum oven for 12 h. The detailed orthogonal experimental results were discussed in the corresponding Supplementary Figures.

Preparation of self-cleaning and Anti-bacteria nanocoatings

AuKPCN was dispersed in a water/2-propanol mixture (containing 25% 2-propanol and 0.5 wt.% Nafion) to form a stable sol (0.2 mg mL^{-1}). The AuKPCN sol was sonicated for 30 min before

spray coating. The sol was spray-casted onto different substrates (air is used as the flowing gas). The pressure was maintained at 60-70 PSI during the coating process. To improve the film uniformity, an IR light was used to accelerate the evaporation of solvent during the spray-coating process. After casting the AuKPCN film onto the substrate (polyvinyl chloride (PVC) plate, steel plate (5160) and CFOAM PLM), the substrate was dried in a vacuum oven for 24 h.

Preparation of photocatalytic bags for solar water disinfection

Preparation of photocatalytic sheets: a one-side hydrophobic PTFE membrane (the other side is hydrophilic, treated by piranha solution) was sprayed with AuKPCN and SiO_2 nanoparticles (Brofos-SiO_2-H20, 20 nm in average) for providing gas diffusion pathway[2]. The concentration is 5 mg mL^{-1} of AuKPCN and 1 mg mL^{-1} of SiO_2, dispersed in 2-propanol with addition of 0.1 wt.% Nafion. During spray-coating, the hydrophilic side of the PTFE membrane was used to support the catalytic layer. The spay pressure was maintained at 50-60 PSI during the process. To improve the film uniformity, an IR light was used to accelerate the evaporation of solvent during the spray-coating process. After casting the suspension onto the substrate, the as-prepared sheet was dried in a vacuum oven for 24 h.

Preparation of photocatalytic bags for solar water disinfection: a commercial PE plastic bag was used for loading the photocatalytic sheets. The bottom surface of the plastic bag was removed. Water proof silicone sealant (Gorilla) was casted at the edge of the photocatalytic sheet. Then, these sheets were pasted directly on the PE bag and settled in air (25 °C).

Photocatalytic reaction toward H_2O_2 and ·OH production

50 mg of photocatalyst was added to 50 mL aqueous solution in a borosilicate glass bottle (φ: 60 mm; capacity: 100 mL), and the bottle was sealed with a rubber septum cap. The catalyst was dispersed by ultrasonication for 15 min, and O_2 was bubbled through the solution for 30 min. The bottle was kept in a temperature-controlled air bath at 25 ± 0.5 °C with air flow and was irradiated using a 300 W Xe lamp ($\lambda \geq 420$ nm, PXE-500, USHIO Inc.) under magnetic stirring. Et-OH, oxalic acid, *p*-hydroxybenzoic acid, salicylic acid, terephthalic acid as typical organic electron donors with different oxidative potentials were used for studying the photo-induced oxidation of AuKPCN. The concertation of the organic donor was 0.01 mol L^{-1} saturated with O_2. The generated amount of H_2O_2 (by photoreduction reaction) was recorded as an indirect probe to investigate the reactivity of the photooxidation reactions. To study ·OH generation in WOR, 50 mg of photocatalyst was added into $AgNO_3$ (0.1 M, 50 mL) solution in a borosilicate glass bottle (φ: 60

mm; capacity: 100 mL). After completely removing O_2 from the reaction system, the mixture was sonicated for 2 min. Then, the system was purged with Ar. The bottle was irradiated by a 300 W Xenon lamp for 5 min and then transferred to ESR immediately for measurement. The light intensity of visible light and infrared-red light ($I_{>420}$) after passing a UV cutoff filter ($\lambda \geq 420$ nm) was firstly measured. Then, a glass filter with $\lambda > 500$ nm was used to replace the UV cutoff filter for measuring the light intensity ($I_{>500}$). The difference between $I_{>400}$ and $I_{>500}$ was used to calibrate the total light intensity. The amount of H_2O_2 produced was determined by a colorimetric method using PACKTEST (WAK-H_2O_2, KYORITSU CHEMICAL-CHECK Lab., Corp.) equipped with a digital PACKTEST spectrometer (ED723, GL Sciences Inc.). To acquire the calibration curves to determine the H_2O_2 concentration, we performed the following steps. Firstly, 10 mL of standard solution of H_2O_2 at concentrations of 0.05, 0.25, 0.5, 0.75, 1, 1.5, 2, 2.5, 3.5 and 5 mg L^{-1} was prepared[3]. Then, 1.5 mL of the standard solution was sucked into the testing bag of the PACKTEST. Subsequently, the bag was shaken for 5-6 times, and let it still for 1 min. The pink solution was transferred to a cuvette for UV test. The absorbance was measured at 540 nm with distilled water as a blank control on a UV/VIS/NIR spectrometer (UV-2600, Shimadzu Co.). The results showed that the absorbance had a good linear relationship with H_2O_2 concentration in the range from 0.05 mg L^{-1} to 5 mg L^{-1} (Supplementary Figure 54), and the regression equation is $y = 0.254x + 0.233$ with $R^2 = 0.999$. A 1260 infinity II (Agilent Technologies, USA) equipped with a C8 reversed-phase column (ZORBAX StableBond C8, 4.6 × 250 mm, 5 μm, 400 bar, 80 Å, 400 bar pressure limit) was used to detect the oxidation products. A 1260 Infinity Variable Wavelength Detector (Agilent Technologies, USA) was also used to identify the separated species at 270 nm. All of the solutions were stored in brown glass bottles and kept in a 4 °C refrigerator for a maximum of two weeks. Fresh working solutions were prepared daily by appropriate dilution of the stock solution. The HPLC eluent was prepared using 7% (v/v) HPLC-grade acetonitrile, 7% methanol (Mallinckrodt, Paris, KY, USA), 0.03 M citric acid (Baker), 0.3 M acetic acid (Riedel-de Haën) and water (86%). The concentration of the dissolved oxygen was determined by a JPB-607A Dissolved Oxygen Meter (INESA Scientific Instrument Co., Ltd, China).

Apparent quantum efficiency

The photocatalytic reaction of H_2O_2 production was carried out in deionized water (1 mL) with photocatalyst (2 mg) in the presence/absence of organic donors (Et-OH, oxalic acid, *p*-hydroxybenzoic acid, salicylic acid, terephthalic acid) in a borosilicate glass bottle. The generated

amount of H_2O_2 (by photoreduction reaction) was recorded as an indirect probe to investigate the reactivity of the photooxidation reactions. The concertation of the organic donor was 0.01 mol L^{-1} saturated with O_2. After ultrasonication and O_2 bubbling, the bottle was irradiated by a Xe lamp for 4 h with magnetic stirring. The incident light was monochromated by band-pass glass filters (Asahi Techno Glass Co.), where the full-width at half-maximum of the light is 11−16 nm. The number of photons that entered the reaction vessel was determined by a 3684 optical power meter (HIOKI E.E. CORPORATION). SA is known to react with ·OH at a rate constant of 2.2×10^{10} M^{-1} s^{-1}[4]. To quantitatively determine the ·OH evolution rate, 0.01 mol L^{-1} salicylic acid (SA) was used as the electron donor to capture ·OH[5], producing 2,3-dihydrobenzoate (2,3-DHBA), 2,5-dihydroxybenzoate (2,5-DHBA) and pyrocatechol[4]. The primary hydroxylated derivatives of salicylic acid (0.01 mol L^{-1}), i.e., 2,3-dihydrobenzoate (2,3-DHBA), 2,5-dihydroxybenzoate (2,5-DHBA) and pyrocatechol, were determined by HPLC to assess, in a relative way, the • OH concentrations[6]. O_2 (8 mg L^{-1}) and 0.01 mol L^{-1} Ag^+ were respectively added into the solution as electron acceptors. The sum of the amount of 2,3-DHBA, 2,5-DHBA, pyrocatechol were used to calculate the absolute amount of ·OH[7].

Instruments

High-resolution transmission electron microscopy, high-angle annular dark field scanning transmission electron microscopy, selected area electron diffraction and energy-dispersive X-ray spectroscopy were performed on a Titan Cubed Themis G2 300 electron microscope at an accelerating voltage of 300 kV. Electron energy loss spectroscopy was conducted using a Quantum ER/965 P detector. The crystalline phases were characterized by a powder X−ray diffraction instrument (MiniFlex II, Rigaku Co.) with CuKα (λ = 1.5418 Å) radiation (cathode voltage: 30 kV, current: 15 mA). Light absorption properties of the samples were determined using the diffuse reflection method on a UV/VIS/NIR spectrometer (UV-2600, Shimadzu Co.) attached to an integral sphere at room temperature. X−ray photoelectron spectroscopy measurements were performed on a Kratos AXIS Nova spectrometer (Shimazu Co., Japan) with a monochromatic Al Kα X-ray source. The binding energy was calibrated by taking the carbon (C) 1s peak of adventitious carbon at 284.6 eV. Valence band X-ray photoelectron spectroscopy was performed on an ESCALAB 250Xi (Thermo Scientific, USA). The equilibration of Fermi level of the instrument was performed by measuring the VB-XPS of Au metal basis as the reference. The Fermi level of the instrument was equilibrated at 4.5 eV. In this case, the numerical value of the

binding energy in the calibrated VB-XPS spectrum is the same as the potential vs. standard hydrogen electrode. Electron spin resonance signals of spin-trapped paramagnetic species with 5,5-diemthyl-1-pyrroline N-oxide (DMPO, methanol solution) were recorded on an A300-10/12 spectrometer. Raman spectra were recorded on a Laser Microscopic Confocal Raman Spectrometer (Renishaw inVia, UK) at 785 nm. The pH of the solution was measured by a pH meter (HORIBA pH meter D-51, HORIBA, Ltd.). The water contact angle was measured by a Theta Flex (Finland, BIOLIN) contact angle analyser. The X-ray absorption spectroscopy for Au K-edge was measured at beamline BL01C at the National Synchrotron Radiation Research Center (NSRRC, Hsinchu, Taiwan, China). The data analysis for the X-ray absorption spectroscopy using IFEFFIT was performed by Demeter system (version 0.9.25).

Electrochemical characterizations

Electrochemical characterizations were conducted on a conventional three-electrode potentiostat setup connected to an electrochemical analyzer (Model 604D, CH Instruments, Inc.). The fluorine-doped tin oxide (FTO) glass of 1 cm × 2 cm in size was covered with photocatalyst that was achieved by first mixing a photocatalyst (100 mg) with ethyl cellulose binder (10 mg) in ethanol (6 mL) for one hour and then depositing the final viscous mixture using a doctor blade method followed by drying at room temperature and further drying at 40 °C overnight in a vacuum oven. The EC system consisted of an FTO glass covered by the photocatalyst, a coiled Pt wire and a saturated Ag/AgCl/KCl (saturated) electrode as the working, counter, and reference electrode, respectively. The area of the electrode for the Mott-Schottky measurements was controlled to be 0.50 cm^2. Mott-Schottky measurements were performed in the potential range from -0.2 V to 0.6 V vs. standard hydrogen electrode (SHE), with an AC voltage amplitude of 5 mV, and in a frequency range from 25 Hz to 250 Hz. Each increase of potential is 0.05 V. The quiet time for each test is 2 s.

***In-situ* FTIR measurements**

In-situ diffuse reflectance infrared Fourier transform spectroscopy (DRIFTS) measurements were performed on a Tensor II FTIR spectrometer (Bruker) equipped with an *in-situ* diffuse reflectance cell (Harrick). Photocatalyst was put into the reaction cell. Firstly, Ar gas (100 mL/min) was blown to remove any residual hydrocarbons and H_2O at 300 ^oC combined with vacuum treatment. The real-time FTIR spectrum after ventilation was used as the background. Secondly,

50 sccm O_2 (humidified) was introduced into the reaction cell filled with Et-OH (10% v/v) aqueous solution. *In-situ* FTIR spectra of PCN, AuPCN, KPCN and AuKPCN exposed to humid O_2 under light irradiation for 30 mins were recorded. The FTIR spectra were recorded every 1 min in the first 5 min and every 2 min between 5 and 25 min with the same gas flux after turning off the light. The *in-situ* FTIR spectra were obtained by subtracting the spectra obtained at a certain time point to the spectrum obtained at the time point of 0. As a result, the typical vibrations of PCN and KPCN were eliminated by this processing. The signal changes reflected by the products produced during photoreaction could be captured. The IR scanning range was from 4000 to 600 cm^{-1}.

Isotopic experiments with D_2O and Et-OD

60 mg of AuKPCN was dispersed in 30 ml of D_2O with Et-OH (10% v/v) via sonication for 15 min. Subsequently, O_2 gas was bubbled into the solution. Then, the system was completely sealed and irradiated by visible light (AM 1.5). After a certain time interval (10 min, 20 min, 30 min, 40 min, 50 min and 60 min), the solution was extracted for measuring the concentration of H_2O_2. The H_2O with Et-OD (10% v/v) were also used to investigate whether the active H in Et-OH participated in the proton transfer during the ORR process.

Solar water disinfection and photodegradation of organic compounds

Different kinds of bacteria, including *E. coli* (ATCC K-12), were cultured to log phase and precipitated by centrifugation at 3000 rpm. Then, the bacteria were washed by phosphate-buffered saline (PBS) twice and dispersed in PBS (10^9 CFU mL^{-1}). The starting concentration of bacteria was adjusted to be 10^6 CFU mL^{-1}, and the bacteria concentration at each time point of the experiment was standardized to the starting concentration. Photocatalytic disinfection was performed under AM 1.5 irradiation. The water volume was 100 mL, and the depth of the aqueous solution was 5 mm. Bacteria concentrations were measured by standard spread-plating techniques with different irradiation durations. Each sample was serially diluted, and each dilution was plated in quintuplicate onto solid medium and incubated at 37 ^oC for 16 h. The solar-disinfection experiments were conducted in quintuplicate (n = 3). AM 1.5 light source was also used for measuring the activity in oxalic acid and *p*-hydroxybenzoic acid as AM 1.5 irradiation represents the closest condition for natural sunlight.

Details for TDDFT calculations

The optimization and frequency combined with the vertical excitation properties were performed via time-dependent density functional theory (TDDFT) in the Gaussian 09 program S2, which was carried out by utilizing wb97xd/6-311g(d) level of theory for C, N and H elements and SDD for Au element. 3 monolayer cluster models were optimized to represent the major surface properties of Au sites in PCN and KPCN. The charges of monolayer cluster models were settled in consideration of the oxidation state of Au and K based on the experimental results as follows: 0 for AuK-PHI, K-PHI and Melon; and +1 for Melon_Au. To give a comprehensive understanding of the relationships between the electronic configuration during excitation and the realistic experimental results, 50 excited states (ES) of these three cluster models were used to simulate the UV absorption spectra. Note that the absorption edge of the simulated UV spectra is usually larger than that of the experimental ones because of the following two reasons: (1) To simulate the charge-transfer properties of the model with high qualities, function of wb97xd, a function including large amount of Hartree–Fock exchange, was used. These exchange functions usually overestimate the excitation energies, as well as the simulated HOMO-LUMO gap[8-10]; (2) In the solid state, p-conjugated molecules adjacent to the one carrying a charge do strongly polarize, an effect that stabilizes the cationic and anionic states (each generally by about one eV in *p*-conjugated materials). In this case, the band gap is typically considerably smaller in energy than the molecular fundamental gap, as well as the optical gap[10]. Since the inevitable system error could not be eliminated, the possible simulated ES that contributed to H_2O_2 production (corresponding to the spectra from 420 nm to 470 nm) was confirmed by comparing the experimental spectra with the simulated ones. Then, the transition density of electrons/holes were considered at all these ES.

For analysis of the excitation and charge transfer properties, Multiwfn Ver. 3.6 (released on May 21, 2019) was performed. Visualization of hole, electron and transition density was also performed by Multiwfn: functions of *IOp(9/40 = 3)* were set during the vertical excitation based on TDDFT calculation. The electron distributions at these ES were presented as heatmaps by combination of GaussView and Multiwfn. The iso surface of LUMO orbitals were presented by setting the isovalue of 0.05.

We defined a weighted arithmetic electron-hole strength and a normalized charge separation index for evaluating the relative contribution of orbitals contributed by each atom in the model as follows:

$$I_{WA-x} = \frac{I_{osillitor}}{I_{Mstongest}} \times C \times I_{H-x}$$

$$D_{A-x} = \frac{I_{osillitor}}{I_{Mstongest}} \times C \times D_x$$

where I_{WA-x} is the weighted arithmetic electron/hole strength of an atom in the model;

D_{A-x} is the weighted arithmetic distance between the center of electron and hole in the model;

$I_{osillitor}$ is the absolute intensity of oscillator strength obtained from TDDFT calculation;

$I_{Mstongest}$ is the maximum molar absorption coefficient;

C is a constant regarding to the size of the model. In our case, C is set as 100000;

I_{H-x} is the electron hole distribution percentage of the atom based on the population analysis of the model;

D_x is the distance between the center of electron and hole at the excited states x;

I_{WA-x} can be used for estimating the charge concentration at a certain point or molecular fragment in each excited state;

D_{A-x} can be used for estimating the level of charge separation in each excited state.

Note that only separated charges with high charge concentration could participate in the photocatalytic reaction.

$$I_{WD} = I_{WA-x} \times D_{A-x}$$

The sum of I_{WD} of 50 excited states is used to define the charge concentration and charge separation in a certain site or a certain fragment.

Data Availability

All source data for Figures in the manuscript, extended data, and supplementary materials. The data that support the findings of this study are available from the corresponding author upon reasonable request.

Methods-only references

1. Wang, X. et al. A metal-free polymeric photocatalyst for hydrogen production from water under visible light. *Nat. Mater.* **8**, 76-80 (2009).
2. Xiong, A. et al. Fabrication of photocatalyst panels and the factors determining their activity for water splitting. *Catal. Sci. Technol.* **4**, 325-328 (2014).
3. Teng, Z. et al. Atomically dispersed antimony on carbon nitride for the artificial photosynthesis of hydrogen peroxide. *Nat. Catal.* **4**, 374-384 (2021).

4. Gligorovski, S., Strekowski, R., Barbati, S. & Vione, D. Environmental implications of hydroxyl radicals (·OH). *Chem. Rev.* **115**, 13051-13092 (2015).
5. Oturan, M.A. & Pinson, J. Hydroxylation by electrochemically generated OH.bul. radicals. Mono- and polyhydroxylation of benzoic acid: Products and isomer distribution. *J. Phys. Chem.* **99**, 13948-13954 (1995).
6. Zhang, J.-R. et al. Accurate K-edge X-ray photoelectron and absorption spectra of g-C_3N_4 nanosheets by first-principles simulations and reinterpretations. *Phys. Chem. Chem. Phys.* **21**, 22819-22830 (2019).
7. Jen, J.-F., Leu, M.-F. & Yang, T.C. Determination of hydroxyl radicals in an advanced oxidation process with salicylic acid trapping and liquid chromatography. *J. Chromatogr. A* **796**, 283-288 (1998).
8. Lu, T. & Chen, F. Multiwfn: A multifunctional wavefunction analyzer. *J. Comput. Chem.* **33**, 580-592 (2012).
9. Ghuman, K.K. et al. Photoexcited surface frustrated lewis pairs for heterogeneous photocatalytic CO_2 reduction. *J. Am. Chem. Soc.* **138**, 1206-1214 (2016).
10. Bredas, J.-L. Mind the gap! *Mater. Horiz.* **1**, 17-19 (2014).

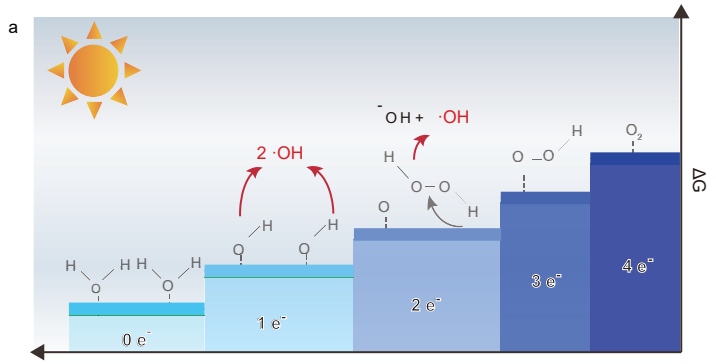

Electron transfer numbers (n) on a photocatalyst

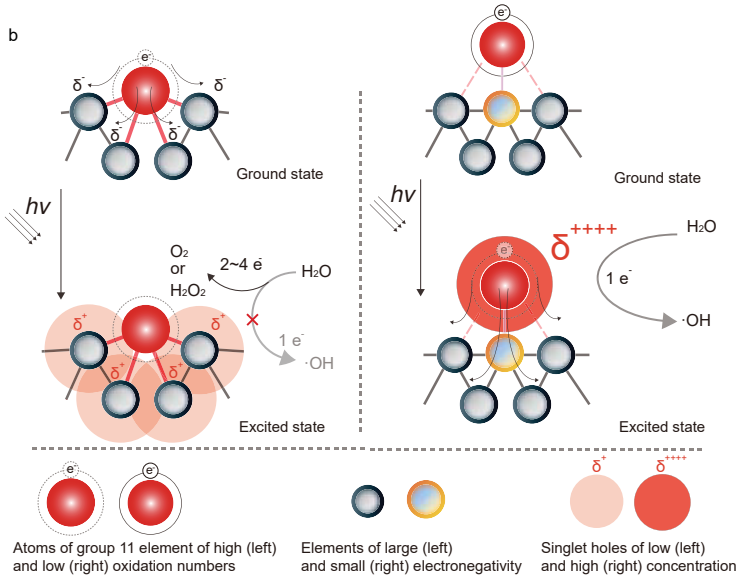

Atoms of group 11 element of high (left) and low (right) oxidation numbers

Elements of large (left) and small (right) electronegativity

Singlet holes of low (left) and high (right) concentration

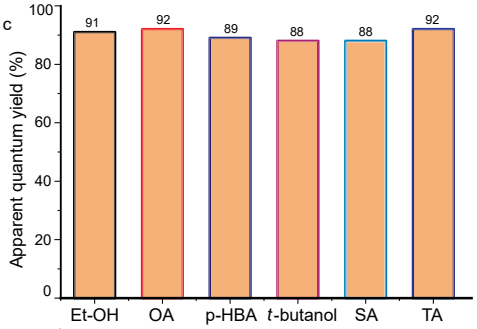

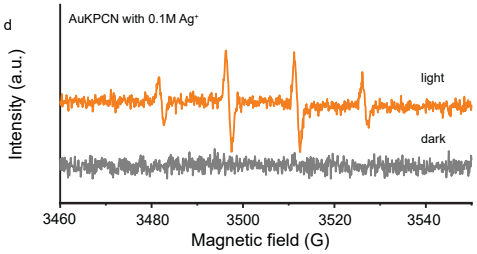

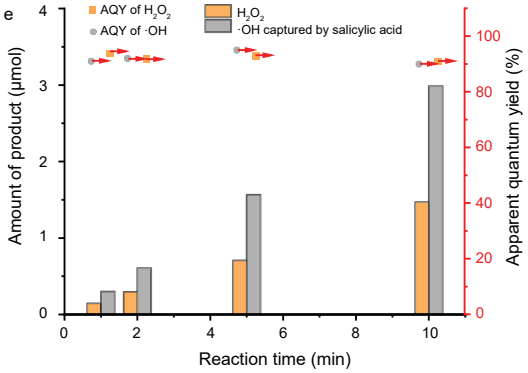

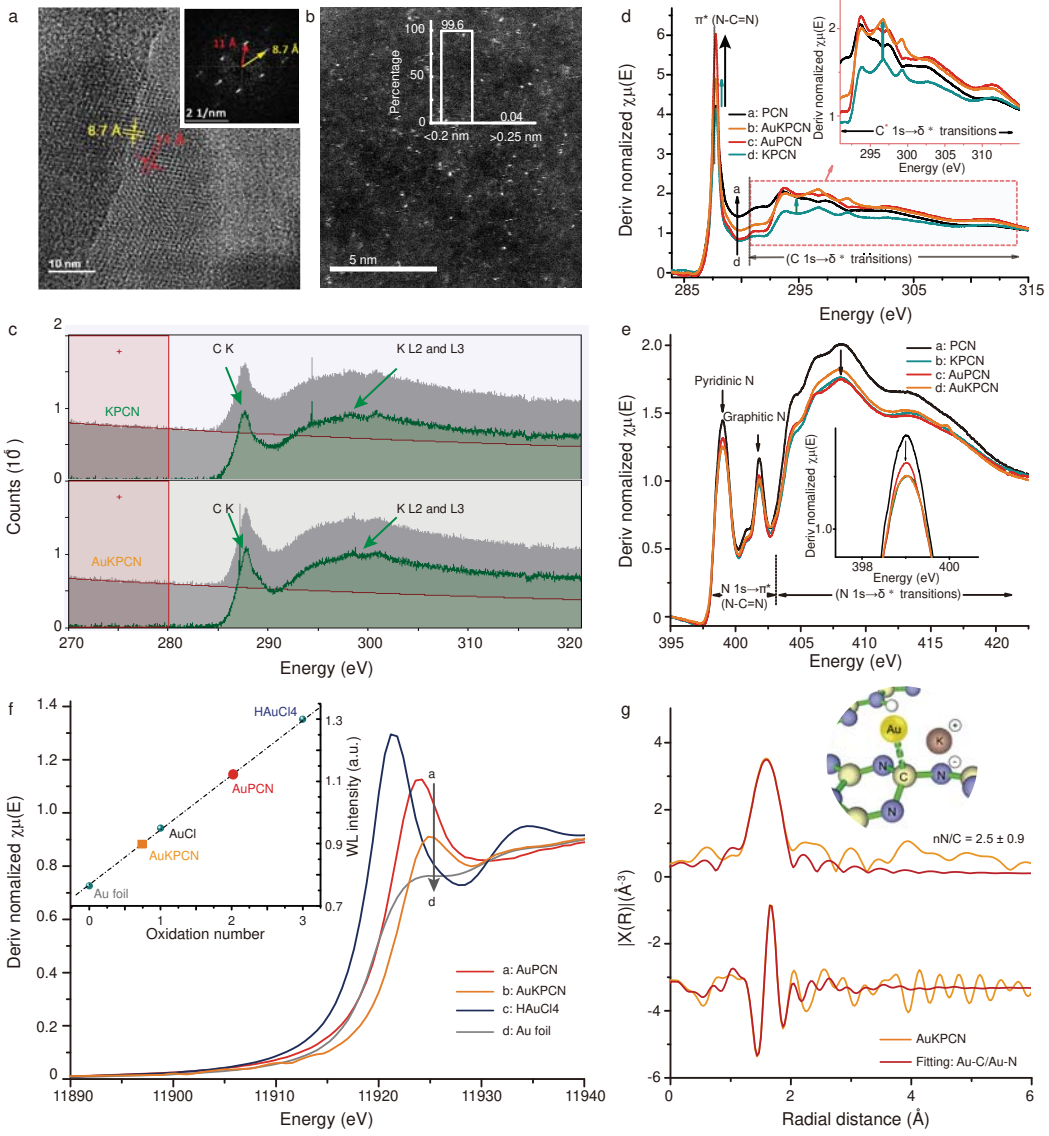
a
11 A
8.7 A
2 1/nm
8.7 A
11 A
10 nm
b
100
50
0
Percentage
99.6
0.04
<0.2 nm
>0.25 nm
5 nm
d
π* (N-C=N)
a: PCN
b: AuKPCN
c: AuPCN
d: KPCN
Deriv nomalized χμ(E)
C´ 1s→δ * transitions
Energy (eV)
(C 1s→δ * transitions)
c
C K
K L2 and L3
KPCN
AuKPCN
Counts (1δ)
Energy (eV)
e
Pyridinic N
Graphitic N
N 1s→π*
(N-C=N)
(N 1s→δ * transitions)
f
HAuCl4
AuPCN
AuCl
AuKPCN
Au foil
Oxidation number
WL intensity (a.u.)
a: AuPCN
b: AuKPCN
c: HAuCl4
d: Au foil
g
Au
K
N
C
nN/C = 2.5 ± 0.9
|X(R)|(Å-3)
AuKPCN
Fitting: Au-C/Au-N
Radial distance (Å)

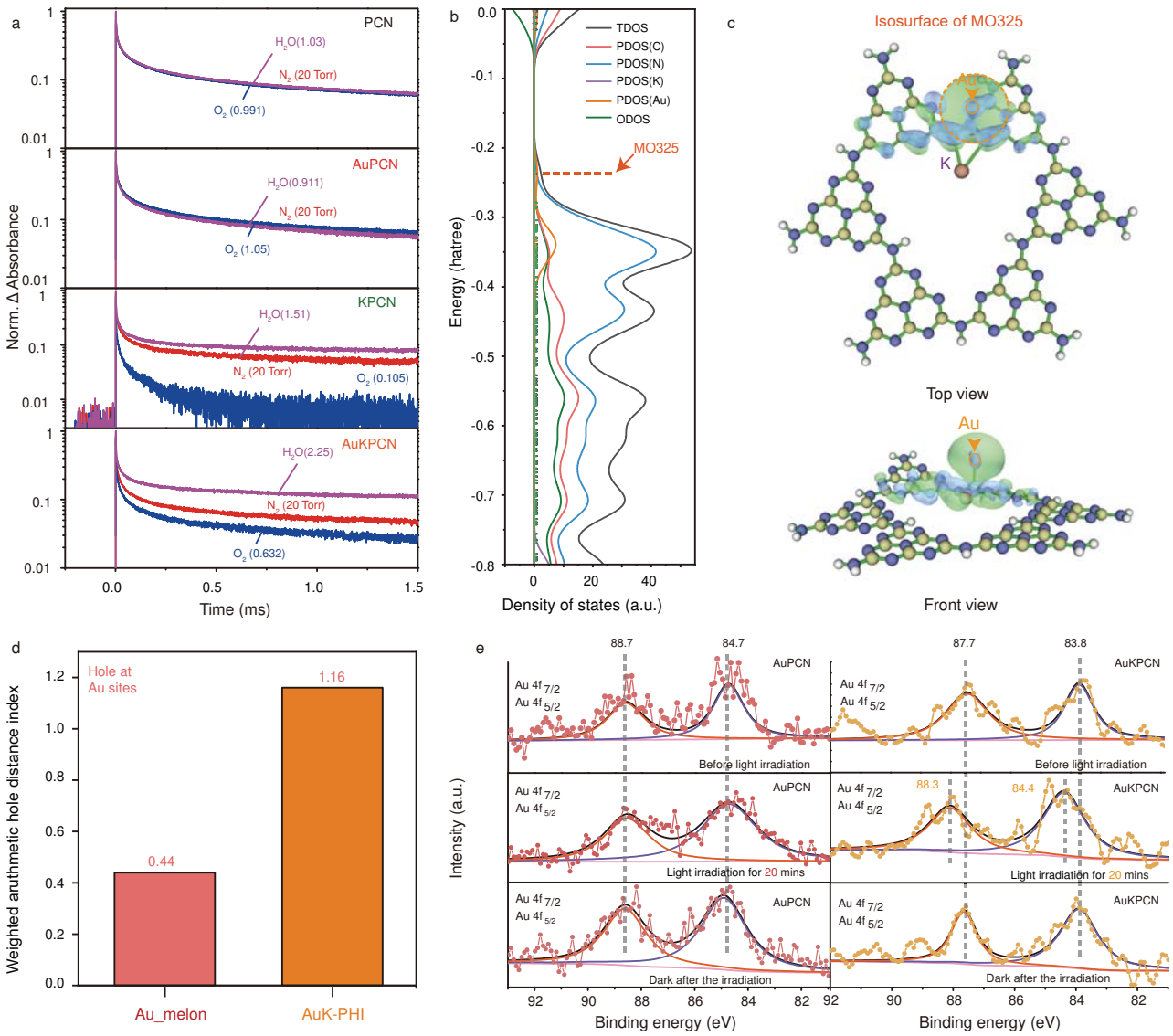
a
PCN
H2O(1.03)
N2 (20 Torr)
O2 (0.991)
AuPCN
H2O(0.911)
N2 (20 Torr)
O2 (1.05)
KPCN
H2O(1.51)
N2 (20 Torr)
O2 (0.105)
AuKPCN
H2O(2.25)
N2 (20 Torr)
O2 (0.632)
Norm. Δ Absorbance
Time (ms)
b
TDOS
PDOS(C)
PDOS(N)
PDOS(K)
PDOS(Au)
ODOS
MO325
Energy (hatree)
Density of states (a.u.)
c
Isosurface of MO325
Au
K
Top view
Au
Front view
d
Hole at
Au sites
0.44
1.16
Weighted aruthmetic hole distance index
Au_melon
AuK-PHI
e
88.7
84.7
AuPCN
87.7
83.8
AuKPCN
Au 4f 7/2
Au 4f 5/2
Before light irradiation
Light irradiation for 20 mins
88.3
84.4
Dark after the irradiation
Intensity (a.u.)
Binding energy (eV)

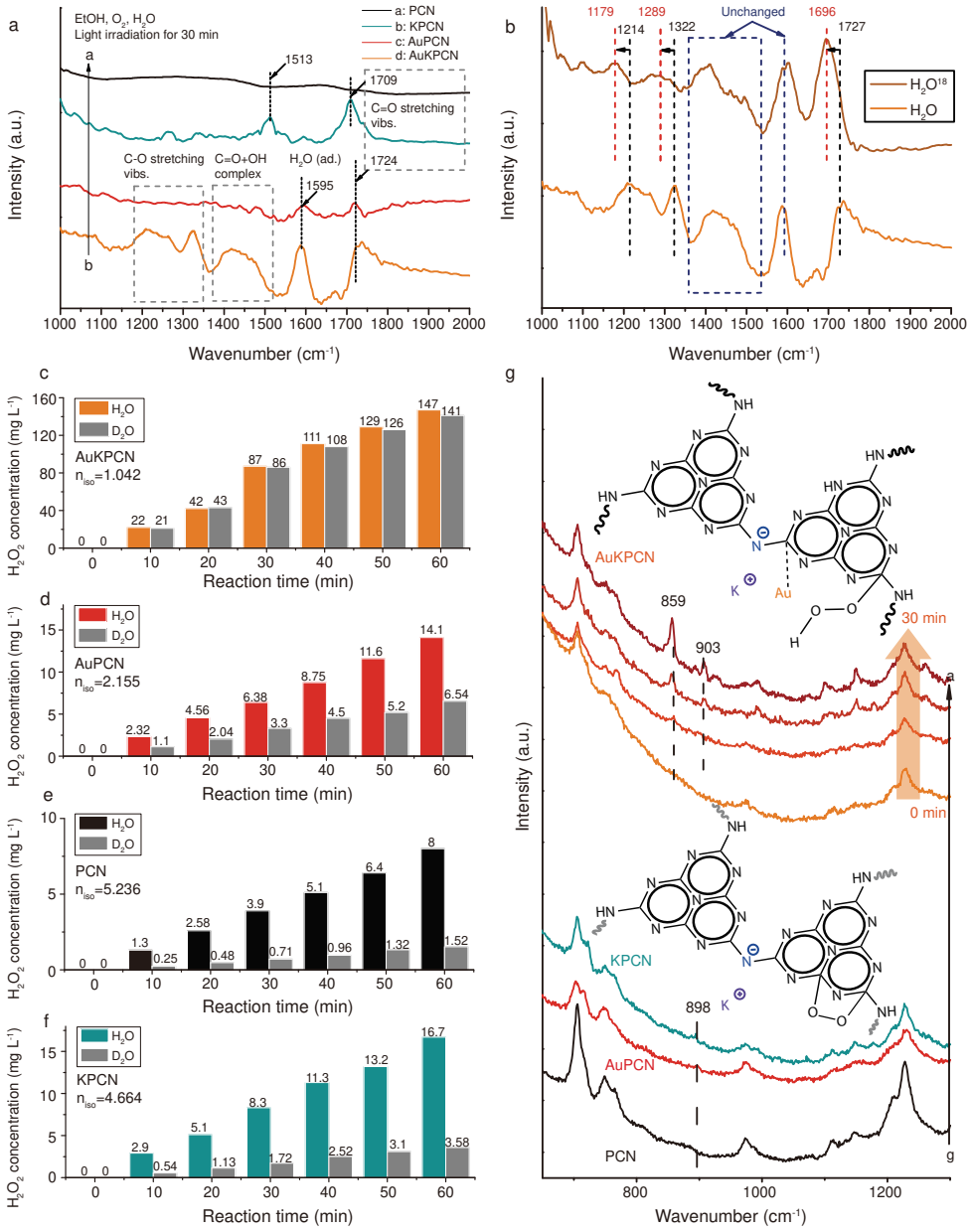
a
EtOH, O2, H2O
Light irradiation for 30 min
a: PCN
b: KPCN
c: AuPCN
d: AuKPCN
1513
1709
C=O stretching vibs.
C-O stretching vibs.
C=O+OH complex
H2O (ad.)
1595
1724
Intensity (a.u.)
Wavenumber (cm-1)
b
1179
1289
1214
1322
Unchanged
1696
1727
H2O18
H2O
Intensity (a.u.)
Wavenumber (cm-1)
c
H2O
D2O
AuKPCN
nIso=1.042
H2O2 concentration (mg L-1)
Reaction time (min)
d
AuPCN
nIso=2.155
e
PCN
nIso=5.236
f
KPCN
nIso=4.664
g
AuKPCN
KPCN
AuPCN
PCN
859
903
898
30 min
0 min
K
Au
Intensity (a.u.)
Wavenumber (cm-1)

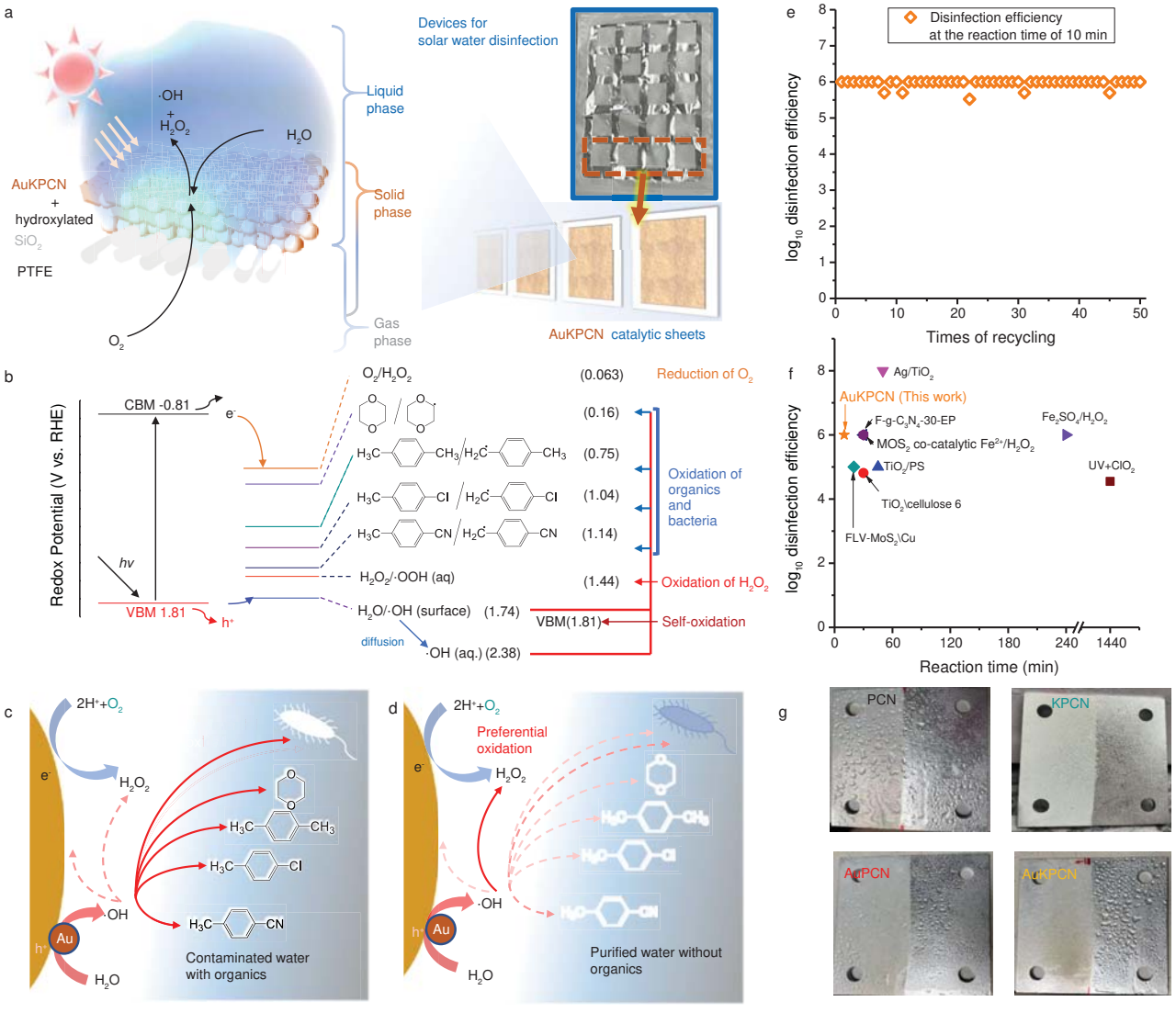
a
·OH + H_2O_2
H_2O
AuKPCN + hydroxylated SiO_2
PTFE
O_2
Liquid phase
Solid phase
Gas phase
Devices for solar water disinfection
AuKPCN catalytic sheets
b
Redox Potential (V vs. RHE)
CBM -0.81
e⁻
hv
VBM 1.81
h⁺
O_2/H_2O_2
(0.063)
Reduction of O_2
(0.16)
(0.75)
(1.04)
(1.14)
Oxidation of organics and bacteria
H_2O_2/·OOH (aq)
(1.44)
Oxidation of H_2O_2
H_2O/·OH (surface)
(1.74)
VBM(1.81)
Self-oxidation
diffusion
·OH (aq.) (2.38)
e
Disinfection efficiency at the reaction time of 10 min
log_{10} disinfection efficiency
Times of recycling
f
Ag/TiO_2
AuKPCN (This work)
F-g-C_3N_4-30-EP
Fe_2SO_4/H_2O_2
MOS_2 co-catalytic Fe^{2+}/H_2O_2
TiO_2/PS
UV+ClO_2
TiO_2\cellulose 6
FLV-MoS_2\Cu
log_{10} disinfection efficiency
Reaction time (min)
c
2H⁺+O_2
e⁻
H_2O_2
·OH
Au
h⁺
H_2O
Contaminated water with organics
d
2H⁺+O_2
Preferential oxidation
e⁻
H_2O_2
·OH
Au
h⁺
H_2O
Purified water without organics
g
PCN
KPCN
AuPCN
AuKPCN

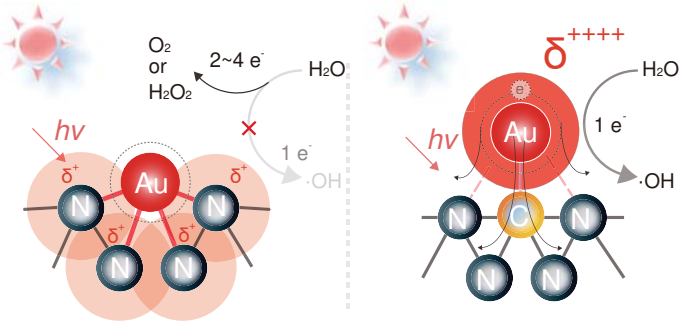
O2
or
H2O2
2~4 e-
H2O
1 e-
·OH
hv
δ+
Au
N
δ++++
e-
C

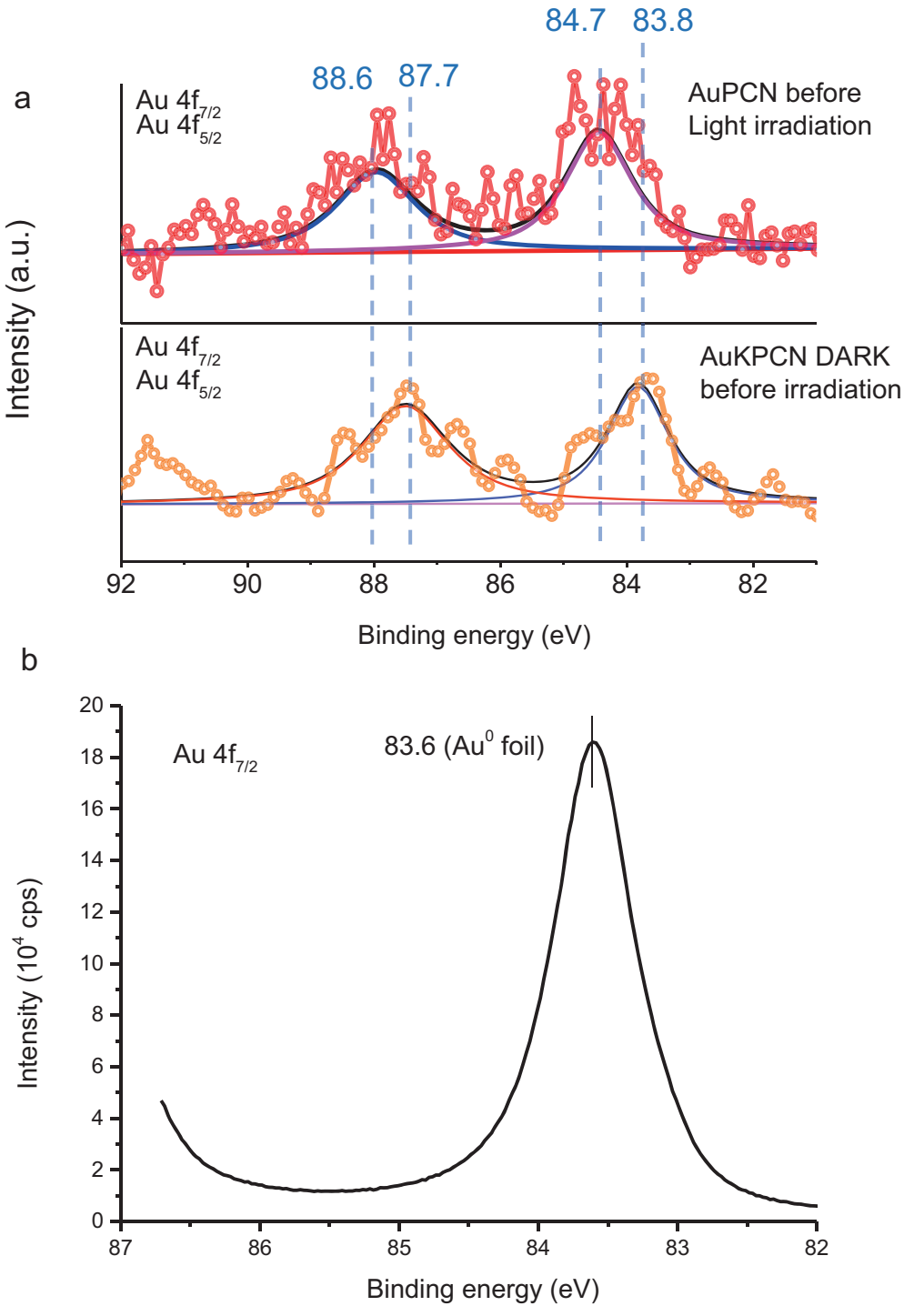
a
84.7
83.8
88.6
87.7
Au 4f7/2
Au 4f5/2
AuPCN before
Light irradiation
Au 4f7/2
Au 4f5/2
AuKPCN DARK
before irradiation
Intensity (a.u.)
92
90
88
86
84
82
Binding energy (eV)
b
Au 4f7/2
83.6 (Au0 foil)
Intensity (10^4 cps)
20
18
16
14
12
10
8
6
4
2
0
87
86
85
84
83
82
Binding energy (eV)

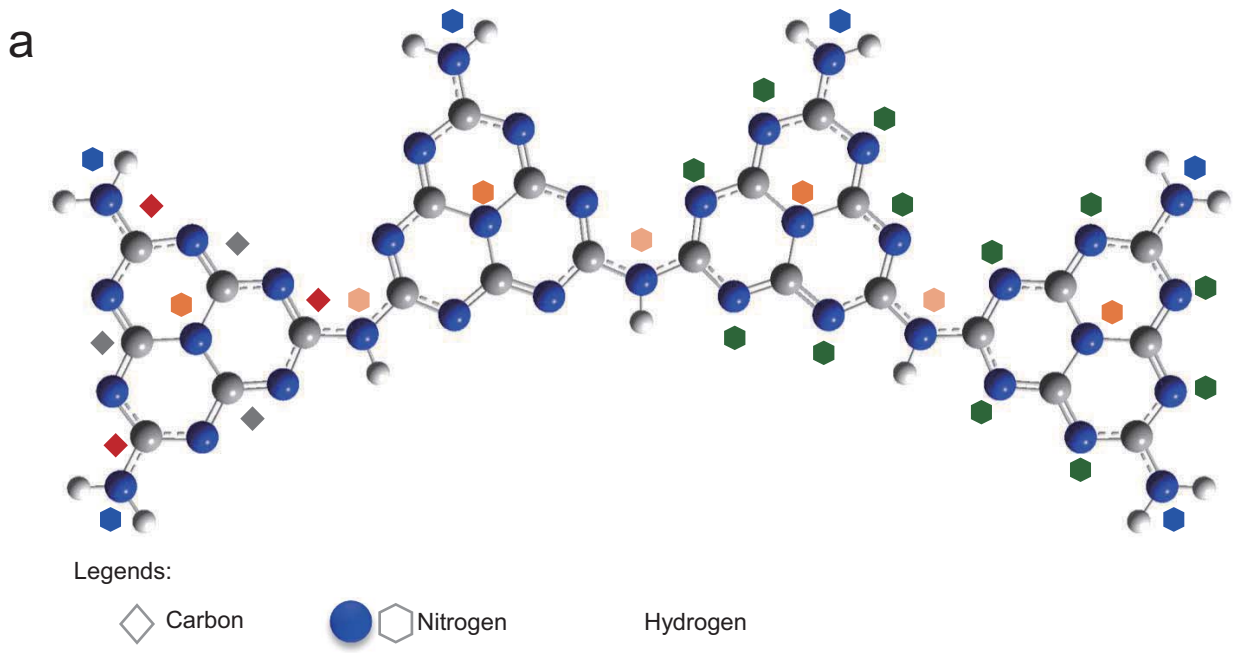
a
Legends:
Carbon
Nitrogen
Hydrogen

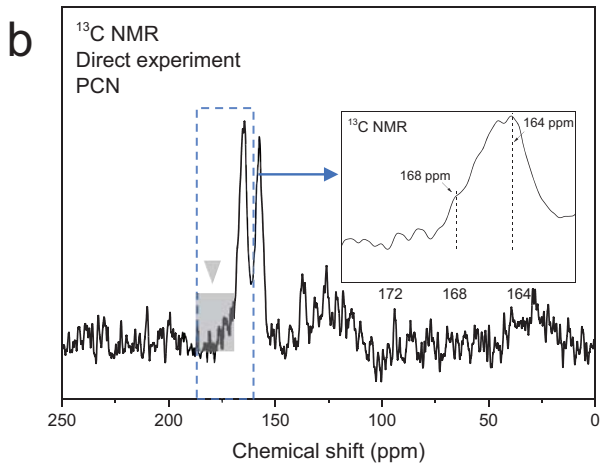
b
13C NMR
Direct experiment
PCN
13C NMR
164 ppm
168 ppm
172
168
164
250
200
150
100
50
0
Chemical shift (ppm)

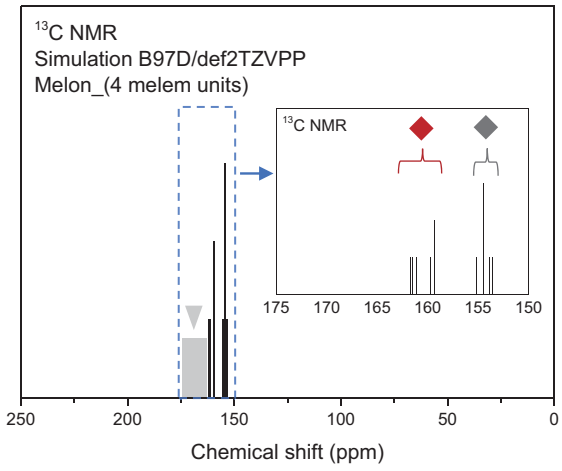
c
13C NMR
Simulation B97D/def2TZVPP
Melon_(4 melem units)
13C NMR
175
170
165
160
155
150
250
200
150
100
50
0
Chemical shift (ppm)

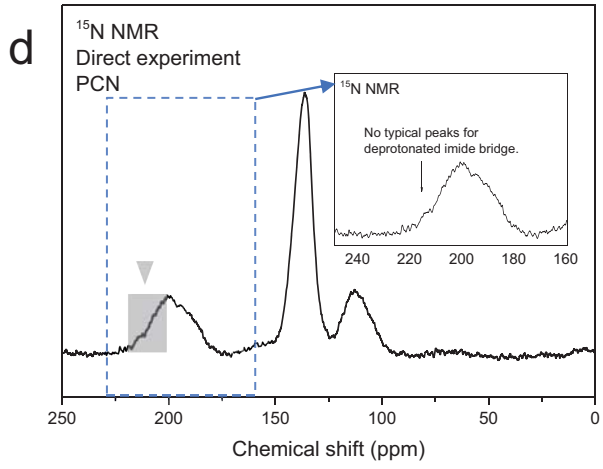
d
15N NMR
Direct experiment
PCN
15N NMR
No typical peaks for
deprotonated imide bridge.
240
220
200
180
160
250
200
150
100
50
0
Chemical shift (ppm)

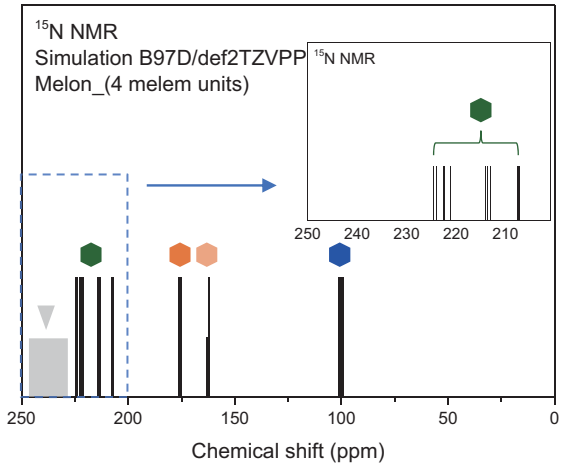
e
15N NMR
Simulation B97D/def2TZVPP
Melon_(4 melem units)
15N NMR
250
240
230
220
210
250
200
150
100
50
0
Chemical shift (ppm)

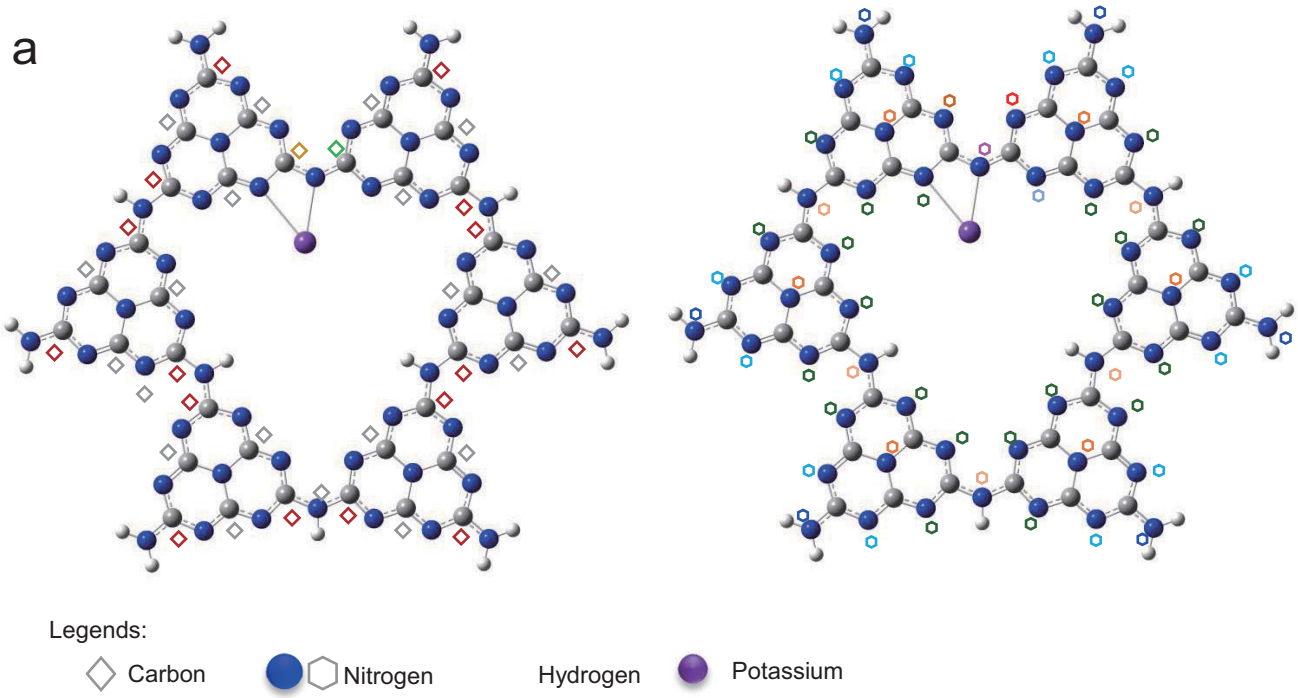
a
Legends:
Carbon
Nitrogen
Hydrogen
Potassium

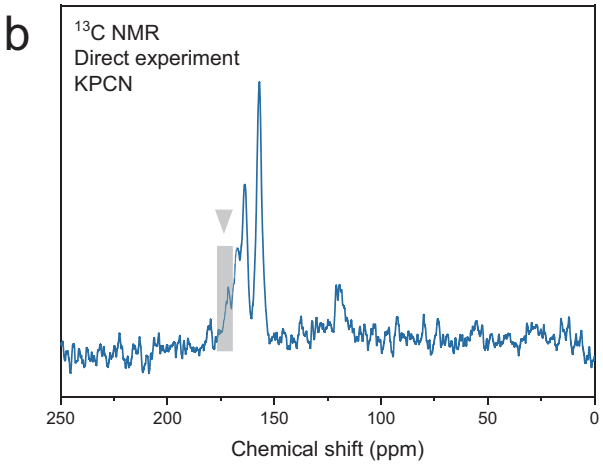
b
13C NMR
Direct experiment
KPCN
250
200
150
100
50
0
Chemical shift (ppm)

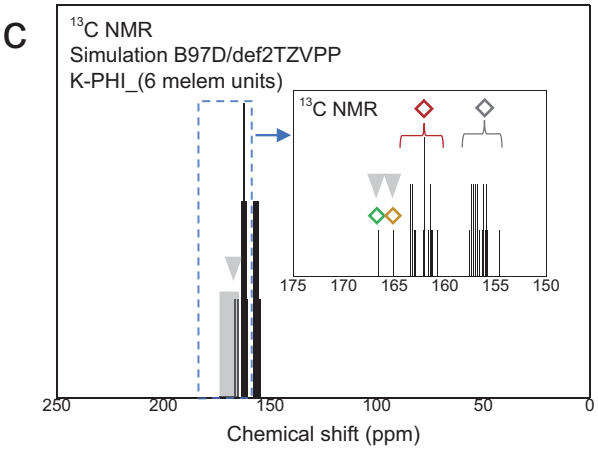
c
13C NMR
Simulation B97D/def2TZVPP
K-PHI_(6 melem units)
13C NMR
175
170
165
160
155
150
250
200
150
100
50
0
Chemical shift (ppm)

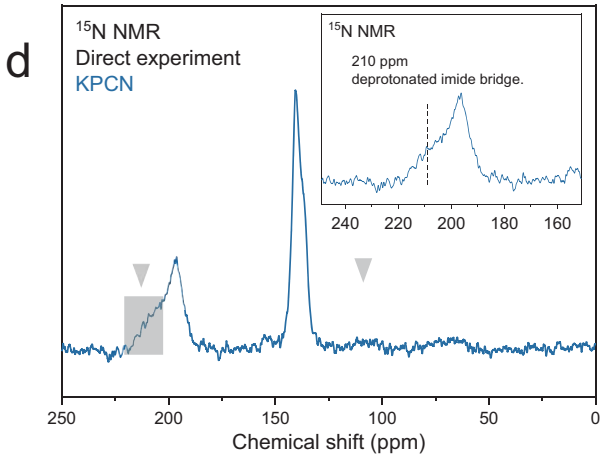
d
15N NMR
Direct experiment
KPCN
15N NMR
210 ppm
deprotonated imide bridge.
240
220
200
180
160
250
200
150
100
50
0
Chemical shift (ppm)

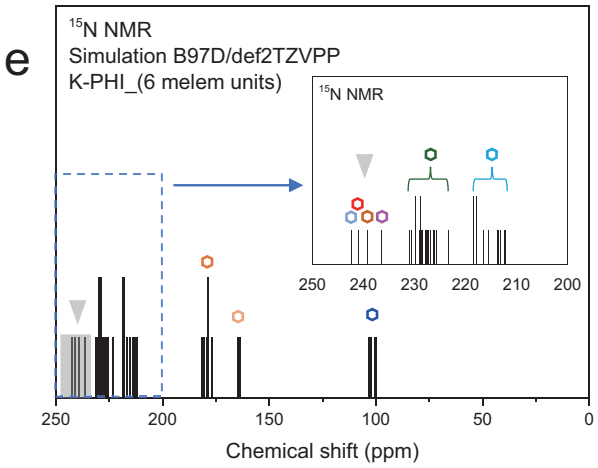
e
15N NMR
Simulation B97D/def2TZVPP
K-PHI_(6 melem units)
15N NMR
250
240
230
220
210
200
250
200
150
100
50
0
Chemical shift (ppm)

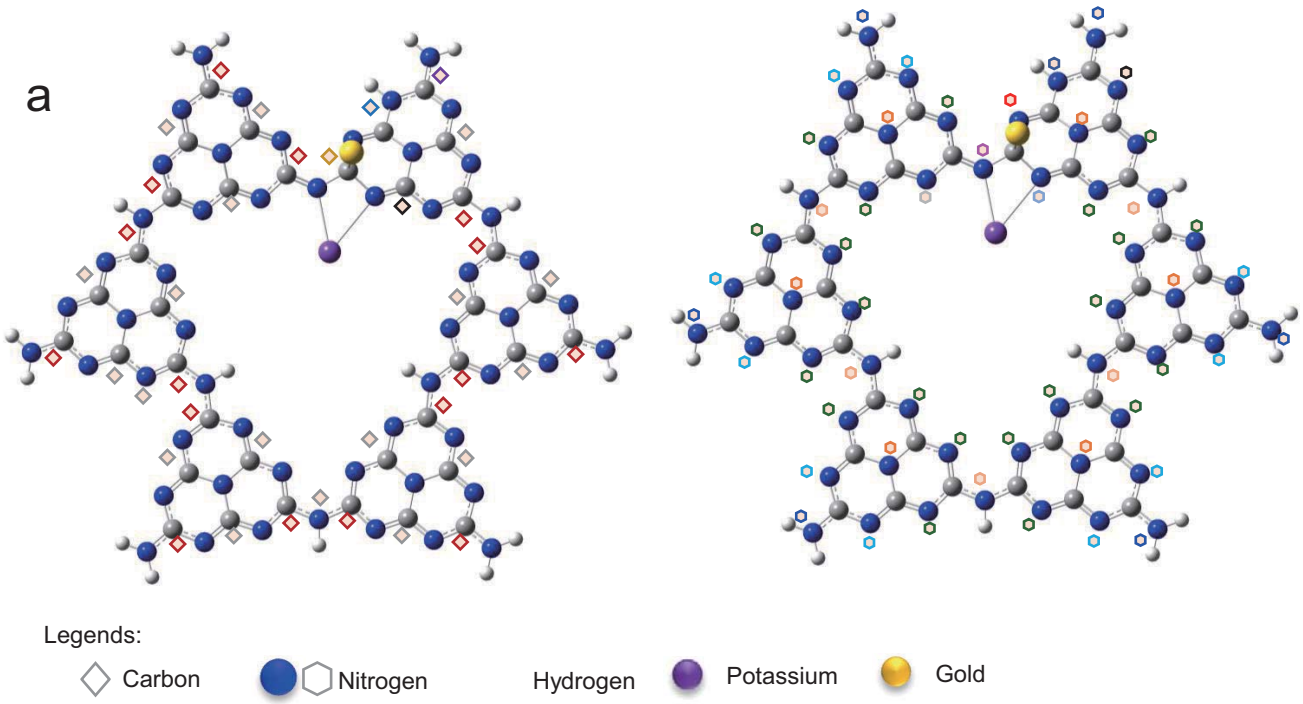
a
Legends:
Carbon
Nitrogen
Hydrogen
Potassium
Gold

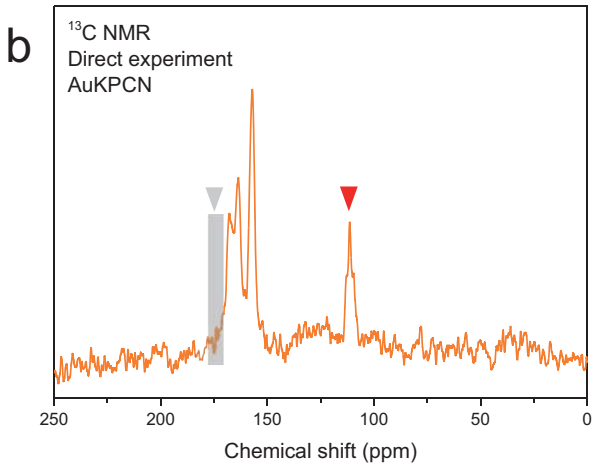
b
13C NMR
Direct experiment
AuKPCN
250
200
150
100
50
0
Chemical shift (ppm)

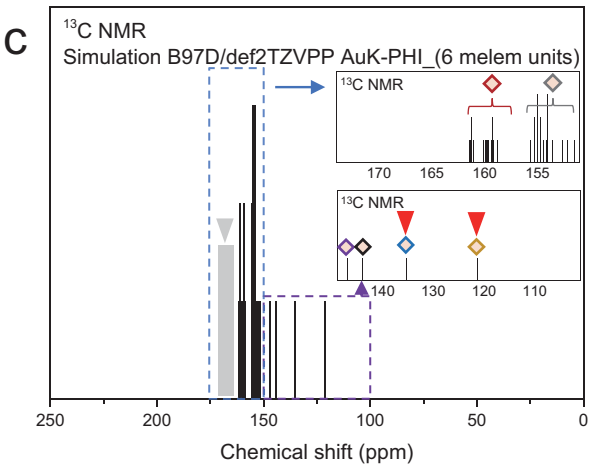
c
13C NMR
Simulation B97D/def2TZVPP AuK-PHI_(6 melem units)
13C NMR
170
165
160
155
13C NMR
140
130
120
110
250
200
150
100
50
0
Chemical shift (ppm)

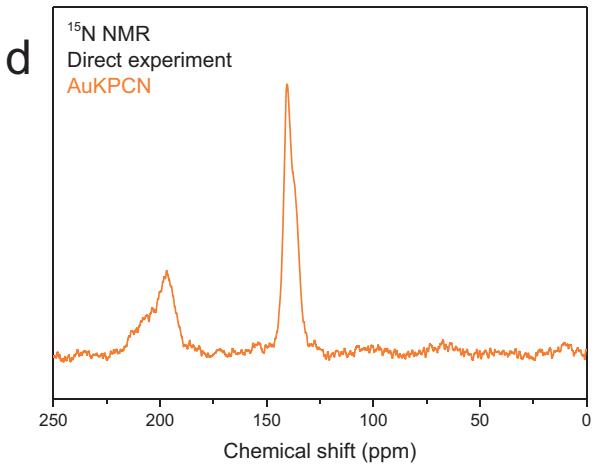
d
15N NMR
Direct experiment
AuKPCN
250
200
150
100
50
0
Chemical shift (ppm)

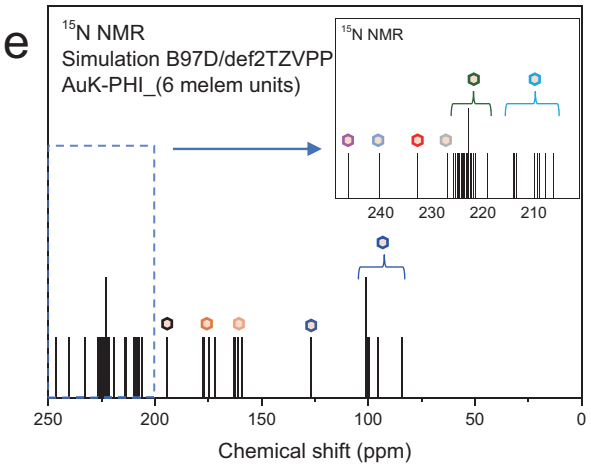
e
15N NMR
Simulation B97D/def2TZVPP
AuK-PHI_(6 melem units)
15N NMR
240
230
220
210
250
200
150
100
50
0
Chemical shift (ppm)

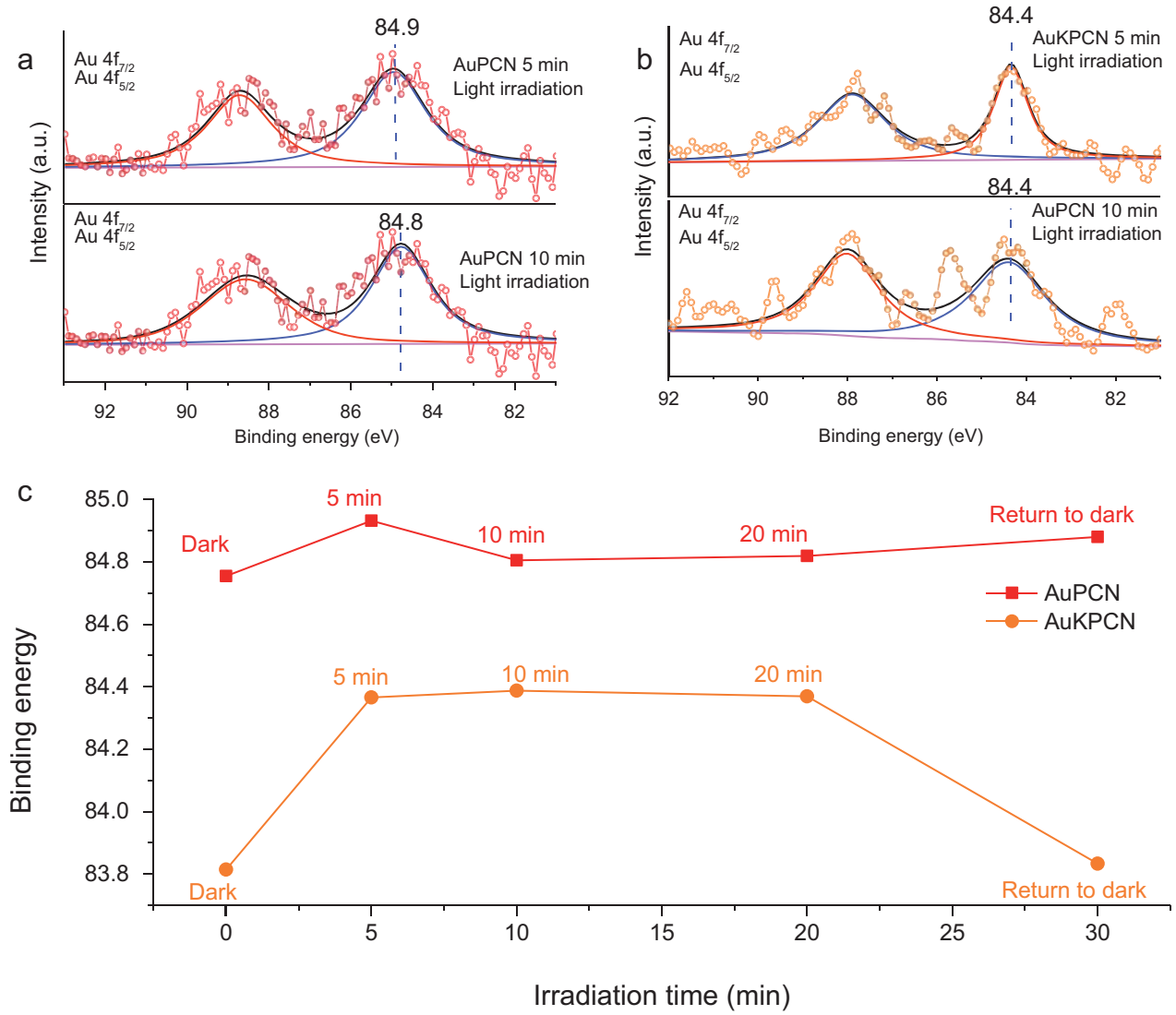
a
Au 4f7/2
Au 4f5/2
84.9
AuPCN 5 min
Light irradiation
Au 4f7/2
Au 4f5/2
84.8
AuPCN 10 min
Light irradiation
Intensity (a.u.)
92
90
88
86
84
82
Binding energy (eV)
b
Au 4f7/2
Au 4f5/2
84.4
AuKPCN 5 min
Light irradiation
Au 4f7/2
Au 4f5/2
84.4
AuPCN 10 min
Light irradiation
Intensity (a.u.)
92
90
88
86
84
82
Binding energy (eV)
c
85.0
84.8
84.6
84.4
84.2
84.0
83.8
Binding energy
Dark
5 min
10 min
20 min
Return to dark
AuPCN
AuKPCN
5 min
10 min
20 min
Dark
Return to dark
0
5
10
15
20
25
30
Irradiation time (min)

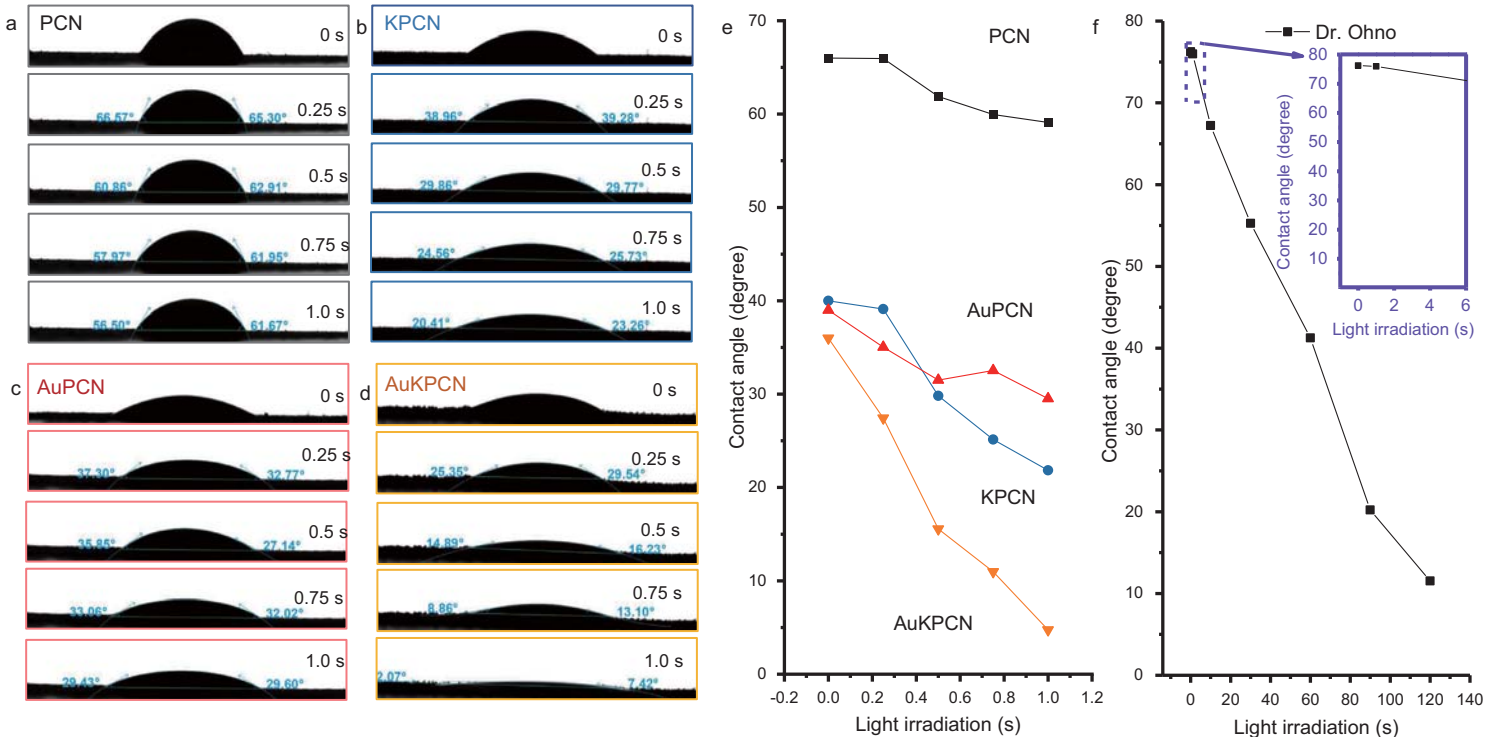
a
PCN
0 s
0.25 s
0.5 s
0.75 s
1.0 s
b
KPCN
0 s
0.25 s
0.5 s
0.75 s
1.0 s
c
AuPCN
0 s
0.25 s
0.5 s
0.75 s
1.0 s
d
AuKPCN
0 s
0.25 s
0.5 s
0.75 s
1.0 s
e
PCN
AuPCN
KPCN
AuKPCN
Contact angle (degree)
Light irradiation (s)
f
Dr. Ohno
Contact angle (degree)
Light irradiation (s)